APPLICATIONS OF LIGHT-MATTER INTERACTION IN NANOSCIENCES

BY
TOMMI HAKALA

Academic Dissertation
for the Degree of
Doctor of Philosophy

To be presented, by permission of the
Faculty of Mathematics and Science
of the University of Jyväskylä,
for public examination in Auditorium FYS-1 of the
University of Jyväskylä on December 18, 2009
at 12 o'clock

Jyväskylä, Finland
December 2009

Preface

The work reviewed in this thesis has been carried out during the years 2005-2009 at the Department of Physics at the University of Jyväskylä.

I want to thank several people for their valuable contribution to this thesis. I was privileged to work with Prof. Henrik Kunttu, Prof. Mika Pettersson, Dr. Anton Kuzyk, Veikko Linko, Antti-Pekka Eskelinen and Hanna-Mari Tikkanen. Also my dear friends Dr. Pasi Kivinen, Jari Salmela, Dr. Sampo Tuukkanen, Dr. Panu Koppinen, Marcus Rinkiö, Esa Tarkiainen and Mikko Leskinen deserve special mentioning. Antti Nuottajärvi, Tarmo Suppula and Dr. Pasi Myllyperkiö are acknowledged for their tireless assistance on technical issues.

I also want to thank Prof. Dana Z. Anderson and his group at the University Colorado at Boulder, who were kind enough to teach me optics and atomic physics and for making me feel welcome during my six month visit. In addition, Prof. Matti Kaivola and Dr. Janne Simonen are gratefully acknowledged for their valuable contribution during the revision of this thesis. Dr. Jussi Toppari has been one of the most important persons during the years of my Ph. D. studies. Our endless discussions on both practical and theoretical aspects of my work have been an integral part of my education.

Most of all I want to thank my supervisor Prof. Päivi Törmä. Her insight for both theoretical and experimental physics together with her excellent leadership skills has made it a great pleasure to work under her guidance throughout these years. Finally, I want to thank my family members Sirkka, Juhani and Mika and my love Salla for their support.

Jyväskylä, October 2009

Tommi Hakala

Abstract

In this thesis, light matter interaction in nanoscale has been studied from various aspects. The interaction between surface plasmon polaritons (SPPs) and optically active organic molecules (Rhodamine 6G, Sulforhodamine 101 and Coumarine 30) and semiconducting nanocrystals (quantum dots) is studied in the weak coupling regime. In particular, a photon-SPP-photon conversion with spatially separated in- and outcoupling was demonstrated by using molecules. Also, a frequency down-conversion for propagating SPPs was presented by utilization of vibrational relaxation of organic molecules.

A strong coupling regime was reached for Rhodamine 6G (R6G) and SPP despite the broad absorption linewidth of R6G. This implies that the regime is readily accessible for a wide variety of other molecule-SPP systems as well. In this context, two novel detection methods were introduced, which enable the studies of the system time evolution, information which has been inaccessible in previous studies. For the first time, a quantum mechanical hybridization of two molecular excitations and SPP was presented. Finally, in analogy to tunable-Q optical microcavities, it was shown that the strong coupling can be controlled by adjusting the interaction time between waveguided SPPs and R6G deposited on top of the SPP waveguide. The method allows studying extremely nonadiabatic phenomena in strongly coupled systems, since the interaction time can be controlled with sub-fs precision simply by adjusting the length of the R6G area by standard lithography methods.

Also, a high throughput pattern transfer method for nanoscale objects was introduced, and the proof-of-principle experiment was done using quantum dots. The reported method is extremely robust due to the wealth of trapping force in the system. In addition to high precision and high throughput, the method enables *dynamic control* over the manipulation of objects and transferred pattern; one single universal master stamp can be used to generate any desired multicomponent pattern to

the target plate.

In addition, a method for fabricating ultra high vacuum compatible electrical feedthroughs for Bose-Einstein condensate (BEC) atom trapping chip was introduced. The method takes advantage of the electroplating technology together with the mass fabrication capabilities inherent in UV lithography, enabling the fabrication of on-chip ultra high vacuum sealable feedthroughs, small enough to have dozens of them on a single chip, but large enough to stand high currents necessary for the realization of BEC in such a configuration.

Author's address   Tommi Hakala
Department of Physics
University of Jyväskylä
Finland

Supervisor   Professor Päivi Törmä
Department of Applied Physics
Helsinki University of Technology
Finland

Reviewers   Professor Matti Kaivola
Department of Applied Physics
Helsinki University of Technology
Finland

Dr. Janne Simonen
Optoelectronics Research Centre
Tampere University of Technology
Finland

Opponent   Professor Wolfgang Fritzsche
Institute of Photonic Technology (IPHT), Jena
Germany

List of Abbreviations

SPP	surface plasmon polariton
C30	Coumarine 30
DEP	dielectrophoresis
DNA	deoxyribonucleic acid
ITO	indium tin oxide
PMMA	polymethylmethacrylate
QD	quantum dot
R6G	Rhodamine 6G
SR101	Sulforhodamine 101
UV	ultraviolet
BEC	Bose-Einstein condenstate
DM1	detection 1
DM2	detection 2
DBR	distributed Bragg reflector
VRS	vacuum Rabi splitting
NIL	nanoimprint lithography
μCP	microcontact printing
PDMS	polydimethyl siloxane
FINAL	field induced nanolithography
PBS	phosphate buffered saline
PDACMAC	Poly(Diallyldimethylammonium chloride)
MOT	magneto-optical trap
DI	de-ionized
EIT	eletromagnetically induced transparency

List of Publications

The main results of this thesis have been reported in the following articles:

A.I   A. KUZYK, M. PETTERSSON, J. J. TOPPARI, T. K. HAKALA, H. TIKKA-
NEN, H. KUNTTU, AND P. TÖRMÄ, *Molecular coupling of light with plas-
monic waveguides*. Optics Express **15** (2007) 9908-9917.

A.II   T. K. HAKALA, J. J. TOPPARI, M. PETTERSSON, A. KUZYK, H. TIKKA-
NEN, H. KUNTTU, AND P. TÖRMÄ, *Frequency conversion of propagating
surface plasmon polaritons by organic molecules*. Appl. Phys. Lett. **93** (2008)
123307.

A.III   T. K. HAKALA, J. J. TOPPARI, A. KUZYK, M. PETTERSSON, H. TIKKA-
NEN, H. KUNTTU, AND P. TÖRMÄ, *Vacuum Rabi splitting and strong cou-
pling dynamics for surface plasmon polaritons and Rhodamine 6G molecules*.
Phys. Rev. Lett. **103** (2009) 053602.

A.IV   T. K. HAKALA, V. LINKO, A.-P. ESKELINEN, J. J. TOPPARI, A. KUZYK,
AND P. TÖRMÄ, *Field induced nanolithography for high-throughput pattern
transfer*. Small **5** (2009) 2683.

A.V   H. C. CHUANG, T. K. HAKALA, D. Z. ANDERSON, AND V. M. BRIGHT,
Fabrication of feedthrough atom trapping chips for atomic optics. Transducers
'07 (2007) 1-4244-0842-3/07.

Author's contribution

In I the author participated in the sample fabrication, design and measurements and
developed and realized the method for molecular area deposition.

In II the author made all the samples and measurements and the majority of the
work related to the sample design and data analysis. Further the author participated
in writing the publication.

In III the author made all the samples and the majority of the measurements

and participated in building the measurement setup. The author made the majority of the data analysis and was the main writer of the publication.

In IV the author participated in the measurements and in the sample design and fabrication. He optimized the pattern transfer method and the imaging system. The author participated in the electric field simulations and was the main writer of the publication.

In V the author participated in mapping out the viable methods for the realization of the electrical feedthroughs and participated in the sample design, fabrication and measurements.

Other work to which the author has contributed: T. K. Hakala, J. J. Toppari, and P. Törmä, *A hybrid method for calorimetry with subnanoliter samples using Schottky junctions*, J. Appl. Phys. **101**, 034512 (2007).

Contents

12

Chapter 1

Introduction

1.1 Surface plasmon polaritons (SPPs)

Surface plasmon polaritons are surface electromagnetic waves on a metal/dielectric interface that propagate in a direction parallel to the interface. The electric field associated with SPPs is strongly confined and decays exponentially with increasing distance from the interface (see Fig. 1.1a and b). Many of the appealing features of SPPs come from this confinement: The electric field strength in the vicinity of the interface is enhanced, providing possibilities for fluorescence enhancement [71], surface enhanced Raman studies, single molecule detection [58] and various bioanalytical applications [49]. Also enhanced nonlinear effects such as four wave mixing have been reported [21]. Since photons can be coupled to plasmons and vice versa and the frequency range of SPPs extends over the infrared and visible spectrum, they also provide a new platform for optical communication [59]. However, their decay due to both scattering from the surface imperfections and ohmic losses within the metal has been considered a hindrance to their use. In particular, the short, approximately 10 micrometer propagation distance of SPPs on metal surfaces has limited their applicability in the fields of information transport and processing. A renewed interest towards plasmon based information processing came with the advances of micro- and nanofabrication technologies, which allowed to scale down the metallic structures that could support plasmons to 10-100 nm scale. This allowed for several functional parts to be embedded in length scales well below the characteristic SPP propagation distance. Although SPPs consist of approximately 10^{10} conduction electrons, and as such are true many-body objects, they have been reported to exhibit many unexpected coherent properties even at room temperature. For instance, a photon pair has been shown to maintain entanglement after photon-SPP-photon conversion [26]. Also, stimulated emission of SPPs has been demonstrated [60]. Further, a strong coupling between organic molecules and SPPs at room temperature has been reported, providing interesting possibilities to coherently control the light-matter interaction [9]. In addition, in this thesis the dynamics and the time evolution

of the strongly coupled system in femtosecond timescales has been studied by controlling the interaction time between the SPP and the molecules (see paper **III** of this thesis).
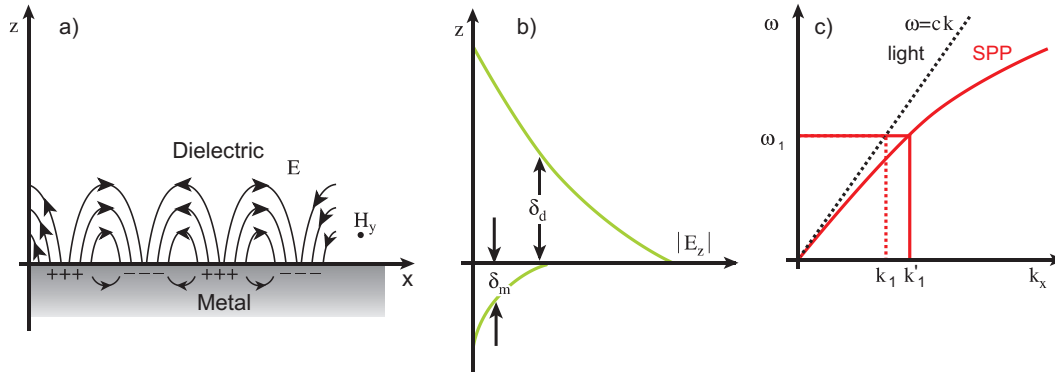

FIGURE 1.1 a) SPPs consist of periodic charge density fluctuations within the metal which are accompanied by the electric field. b) The SPP electromagnetic field decays exponentially with increasing distance into each medium from the interface. c) SPP dispersion relation (red line) with a dispersion of free space photons (black dotted line). To couple light to SPP, the k vector mismatch between k_1 and k_1' should be compensated. This can be done for example by using a prism (Kretschmann configuration). Also a corrugation (individual or periodic) can be used to excite SPPs with light [81]. Adapted with permission from [8].

The electromagnetic field associated with SPP at a dielectric/metal interface can be obtained by solving Maxwell's equations [81]. From the solution one obtains SPP's dispersion relation, that is, the SPP energy (or frequency) as a function of its wave-vector (see Fig. 1.1c),

$$k_{SPP} = \frac{\omega}{c} \sqrt{\frac{\epsilon_d \epsilon_m}{\epsilon_d + \epsilon_m}}, \tag{1.1}$$

where ϵ_d and ϵ_m are the frequency dependent permittivities of the metal and the dielectric, respectively. The permittivities ϵ_d and ϵ_m are required to have opposite signs for SPPs to be possible at the interface. This condition is satisfied for various metal/dielectric pairs, since for metal (dielectric) ϵ_m (ϵ_d) is complex (real) and negative (positive).

The propagation length of SPP ($1/e$ decay length) is given by [81]

$$\delta_{SPP} = \frac{c}{\omega} \frac{|\epsilon_m'|^{1/2} \left(|\epsilon_m'| - \epsilon_d\right)^{3/2}}{\epsilon_d^{3/2} \epsilon_m''}. \tag{1.2}$$

Here ϵ_m' and ϵ_m'' m are the real and imaginary parts of the dielectric function of the metal such that $\epsilon_m = \epsilon_m' + i\epsilon_m''$. For metals with low ohmic losses such as silver, the propagation distances range approximately from 10 μm in the visible frequencies, to millimeter range for the near infrared. The decay lengths of the electric fields within

the dielectric and the metal (see Fig. 1.1b) are of the order of 100 nm and 10 nm, respectively.

1.2 Fluorescence

Fluorescence is generally considered as a process in which a molecule or an atom emits a photon as a result of a decay of the excited electronic state to lower energy state. In practice, fluorescence is often produced by first exciting the electronic state by absorption of a photon. The photon that excites the system is usually higher in energy as compared to the photon emitted by the fluorescence due to nonradiative vibrational relaxation (heat) of the excited electronic state. Fluorescence is an important process not only from the application point of view, but also from the fundamental physical viewpoint: It demonstrates an everyday example of how photons and matter interact. The three processes, absorption, vibrational relaxation and fluorescence have characteristic timescales of 10^{-15} s, 10^{-12} s and 10^{-9} s, respectively (see Fig. 1.2). Since the timescales are separated by several orders of magnitude, it allows to distinguish between the events by timeresolved measurements [61].
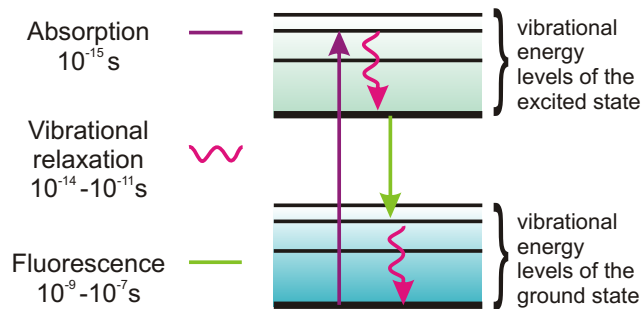
FIGURE 1.2 The schematic energy diagram and the relevant timescales for the absorption, vibrational relaxation and fluorescence.

1.3 Fluorescence near metal surfaces

The fluorescence of an emitter is strongly modified in the vicinity of a metallic surface due to coupling of the electromagnetic field to the conduction electrons of the metal. In particular, the metal surface may alter both the radiative decay rate and the spatial distribution of the emitted radiation. Further, additional non-radiative energy transfer mechanisms become increasingly dominant with decreasing distance. These transfer mechanisms include SPPs and lossy waves. The efficiency of coupling

to different decay channels depends on the details of the system, such as the choice of metal, the frequency, and the orientation of the emitter (which are here treated as radiating dipoles). In Fig. 1.3 is shown the calculated fraction of power dissipated by the emitters to different decay channels [7]. Here, the emitters are positioned above a silver interface and have emission wavelength of 614 nm. The highest coupling to the SPP mode (90 %) comes when the emitters are 200 nm from the surface with their dipole moments oriented perpendicular to the interface. For an isotropic distribution of dipole moment orientations, the coupling to the SPP mode reaches 30 % at a distance of 20 nm from the surface. In the next two chapters, this coupling between emitters, and more precisely organic fluorescent molecules, and SPPs propagating on a plasmonic waveguide, is studied.
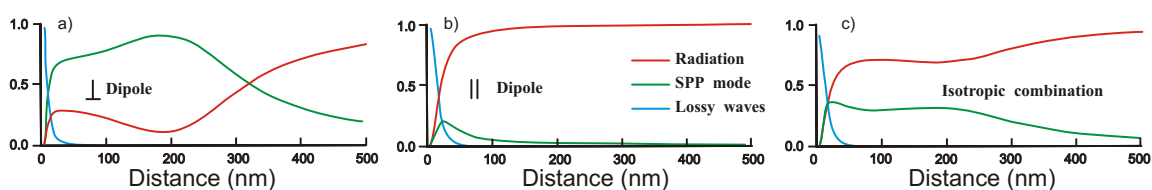

FIGURE 1.3 The relative fractions of the emitter emission to different decay channels. a) for dipoles that are oriented perpendicular to the metal surface. b) for dipoles that are oriented parallel to the metal surface. c) for random orientation of the molecular dipoles. Adapted from [7].

1.4 Particles in nonuniform electric fields

In, general, nonuniform electric fields can be used to exert forces on polarizable particles. Since various insulating, semiconducting and conducting particles exhibit polarizability regardless of their net charge, this method has found diverse applications in atomic physics, biophysics, and nanosciences. The principle of this phenomenon is illustrated schematically in Fig. 1.4. Surface charges are induced on the polarizable object in the electric field, positive on one side of the object and negative on the other. The net force on each side depends on the amount of induced surface charge and the electric field strength. Note that if the field is homogeneous, the forces exerted to the left and right sides of the particle are equal in magnitude but opposite in direction, resulting in a zero net force (see Fig. 1.4 a). However, if the field is nonuniform, there will be a net force acting on a particle (see Fig. 1.4 b). Thus, for this method to be efficient, it is essential to create highly nonuniform fields.

Note that the method does not require any time dependency of the field; however, in the case of charged particle, there will be an additional force acting on a particle due to Coulombic interaction between the charge and the electric field. To average out this effect, a time-varying field is often used. In fact, the method can be
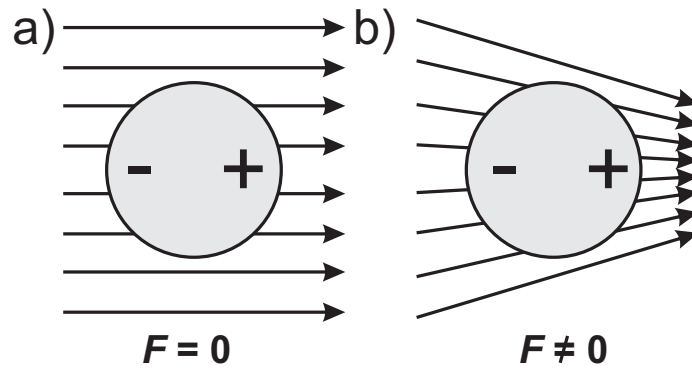
FIGURE 1.4 A net force excerted to a polarizable particle in a uniform electric field averages to zero, while in a nonuniform field there will be a net force.

extended all the way up to the optical frequencies, where light itself can be used to trap and manipulate objects. This can be done with propagating light, as in the case of optical tweezers [43], or with confined light fields as in the case of surface plasmon based trapping [66]. Also individual atoms can be trapped and manipulated by nonuniform light fields. The method is known as *optical dipole trapping* and is frequently applied in cold atom physics and Bose-Einstein condensate related studies. In the paper **IV** of this thesis, we will introduce a case in which nanofabricated electrodes create highly nonuniform fields which are used to trap and manipulate nanoscale objects, a method known as dielectrophoresis.

1.5 Bose-Einstein condensation (BEC)

The behaviour of atoms at very low temperatures lead to extraordinary physical phenomena. When a system of many identical atoms is cooled down close to absolute zero temperature, the overlap of the individual particle wavefunctions results to a collective, coherent state of matter in which quantum effects become apparent on a macroscopic scale. BEC was predicted by Satyendra Nath Bose and Albert Einstein in 1924-25 for photons and later by Einstein for material particles [12, 24]. The first gaseous condensate was produced quite recently (1995) by Eric Cornell and Carl Wieman at the University of Colorado at Boulder NIST-JILA lab, using a gas of rubidium atoms cooled to 170 nK [4]. Cornell, Wieman, and Wolfgang Ketterle at MIT were awarded the 2001 Nobel Prize in Physics for their work on BEC. In the paper **V** of this thesis, a method to fabricate ultrahigh vacuum compatible electrical feedthroughs for atom trapping chip used for BEC, is introduced.

1.6 The connections between the fields

As the papers **I-III** of this thesis describe SPP-molecule interactions, **IV** a novel method for pattern transfer of nanoscale objects and **V** a technical improvement for making electrical connections to the Bose-Einstein condensate setup, this thesis covers a particularly wide variety of different scientific subject areas. At first sight these fields might appear as totally separate. However, each of the papers are closely related to a rapidly growing field of coherent quantum information processing, which is largely relying on the coherent interaction between light and matter. SPPs in conjunction with molecules or quantum dots [3] and SPPs in conjunction with BEC [57], are examples of the current trend of convergence between the fields of plasmonics, BEC and nanoscale emitters such as fluorescent molecules, quantum dots and atoms.

The connection between SPPs and BEC systems. Conventionally Bose-Einstein condensation is realized in a massive vacuum chamber with optical access to allow for precooling of the atoms by utilizing laser light [79]. Magnetic fields that are generated by macroscopic coils, are used to trap and evaporatively cool down the atoms [4]. Currently there exists a strong motivation to miniaturize the BEC systems, and chip-integrated vacuum cells with microscopic current carrying wires have been successfully used for the realization of BEC in microscale [30, 62]. However, the realization of a BEC in nanoscale has not yet been successful, although proposals have been put forward [42, 6]. To create a nanoscale electromagnetic trapping region, one needs to use nanoscale structures. One of the main issues related to nanoscale BEC is the attractive van der Waals forces in the close proximity of the sample surface on which the nanostructures are fabricated [27]. Very recently, a novel method for overcoming these forces was proposed [57]. Surface plasmon resonances supported by metallic nanoparticles could be utilized to exert a repulsive, compensating force to the trapped atoms. The utilization of surface plasmons in the context of atomic physics could therefore open up a route towards nanoscale BEC. Scaling down the BEC to nanoscale is interesting not only from the fundamental physics viewpoint, but would also allow for several BECs in one chip with very small spatial separation. This would be an important milestone if the inherent coherence of BECs are to be used for information processing.

The connection between strongly coupled SPP-molecule systems and strongly coupled BEC systems. Despite the difference in structural complexity of organic molecules compared to atoms, the systems composed of these dissimilar objects share many analogous features. For example, the strong coupling, as reported in the paper **III** for organic R6G molecules and SPPs, will play central role also in the proposal for scaling the BEC for atoms to nanoscale [57]. A striking example of the effects of strong light-matter interaction is the so-called *eletromagnetically induced transparency* (EIT) [31, 11], a coherent effect which makes the optical medium transparent over a very narrow spectral range and leads to strong nonlinearities and extremely low

group velocities of light. Eletromagnetically induced transparency is most often realized in gaseous atom systems [28], and in 1999 it was also reported in Bose-Einstein condensate utilizing strong coupling between the light field and the cooled sodium atoms [32]. Recently, studies have been extended to solid state systems as well, which hold strong potential in terms of practical applications [25]. The strong coupling between SPPs and organic R6G molecules reported in paper **III** of this thesis is one of the first examples of the room temperature coherent interaction between SPPs and molecules and could provide a novel platform for studying coherent phenomena, such as EIT. The great goal of course would be to find a system, in which all the coherent quantum phenomena would be readily accessible at room temperature. If realized this would be revolutionary not only for scientific studies but also for the applications of everyday life.

The motivation for controlling the spatial position of nanoscale emitters. The usage of organic fluorescent molecules and quantum dots is increasing rapidly in the fields of quantum electrodynamics [56], all-optical information processing [40], and plasmonics [3]. Thus it is increasingly important to gain precise control over positioning of these nanoscale emitters. In this thesis, two different methods for depositing optically active material to predefined locations, is introduced. Chapter 2 presents a technique which enables the deposition of several different species of fluorescent molecules or quantum dots onto the predefined positions on the sample by using electron beam or UV lithography. The method allows for 1) patterning of optically active areas with arbitrary shape, with subwavelength dimensions if desired, 2) several different species of molecules to be deposited onto the same sample into any desired configuration, 3) forming hybrid structures, in which molecules and their polymer host are deposited onto the waveguide in periodic subwavelength patterns. Such patterns, but without the plasmonic waveguide, also known as photonic crystals, are presently under intense study due to their capability to modify the optical density of states and to confine light in very small spatial dimensions, making them a promising candidate for optical information processing [80]. The possibility to integrate photonic crystals with plasmonic structures provides interesting prospects to control light-matter interaction in nanoscale [41]. The paper **IV** demonstrates that nonuniform electric fields can be used to manipulate and position quantum dots and other nanoscale objects with high precision and throughput that could prove useful in the realization of novel plasmonic applications, such as a single photon plasmonic transistor [13].

Chapter 2

SPP-molecule interactions in the weak coupling regime

In the next sections we will describe how molecular excitation can be coupled to SPPs. As SPPs are difficult to detect as such, we frequently employ SPP-light conversion to characterize them. This approach is in general very useful due to well developed methodology to characterize photons, in particular their intensity and wavelength. However, attention has to be paid in particular to distinguish the SPP originated photons from ordinary ones (such as background light originating for example from the reflections of the excitation laser or photon emission of the fluorescent molecules used in the experiments). In what follows, we show several methods how these two contributions to the total photon flux can be distinguished. By using these methods, we will show that:

- Molecular emission can be coupled to SPPs.

- These SPPs can be coupled back to photons in two ways:

  - By elastic scattering from a discontinuity in SPP boundary conditions, for example a change in dielectric constant of the dielectric, or abrupt change in metal geometry (the end of the waveguide). In this case the photon energy equals the SPP energy.

  - By using molecules that absorb the incoming SPPs and consequently emit photons. In this case the resulting photon energy usually is lower than the SPP energy, since in the process some fraction of the SPP energy is dissipated to vibrational relaxation of the molecule, a phenomenon also known as Stokes shift and which is frequently encountered in conventional spectroscopy.

- The SPP can be coupled to molecules in such a way that the molecule, by relaxation, re-emits another SPP. In this case the resulting SSP has usually lower

energy than the initial one. The resulting SPP can in turn scatter elastically to a photon from the discontinuity at the sample.

In contrast to free space light, SPPs are bound to the very surface of the metal structures. This difference can be utilized to distinguish the SPP originated photons from the ordinary ones, in particular by designing SPP waveguide samples with carefully chosen geometry.

2.1 Sample fabrication

For the fabrication of the plasmonic waveguide with molecules, a lithography based method that allows deposition of several different types of molecules on top of the plasmonic waveguide structures was developed, see Fig. 2.1. First, 5 µm wide plasmon waveguides (titanium 2 nm and silver 130 nm thick) and alignment marks were fabricated by regular electron beam lithography, thin film evaporation and liftoff techniques onto an indium tin oxide (ITO) coated glass substrate. The molecules (Rhodamine 6G (R6G), Coumarine 30 (C30) or Sulforhodamine 101 (SR 101)) were diluted to SU-8 epoxy-based negative polymer resist (Microchem SU-8 2025), which was spin coated onto the sample. The thickness of the molecular film was controlled by spinning speed and by diluting the resist by a suitable amount of cyclopentanone. Next, electron beam lithography was used to polymerize the resist from the pre-defined locations which was followed by the development of the resist by SU-8 developer (Microchem). The same method was used to deposit a second layer of different molecules onto the sample. The thicknesses of the resulting layers was verified with atomic force microscope. Note that the size and accuracy of positioning of
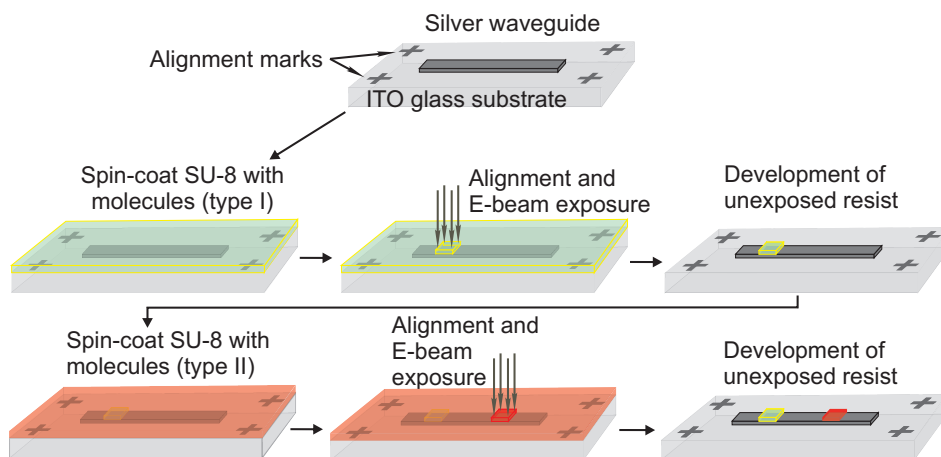

FIGURE 2.1 The schematic of the fabrication of the waveguide and the deposition of the molecules.
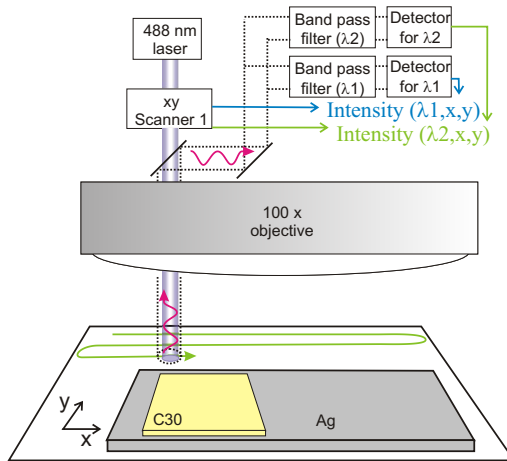
the molecular areas is limited only by the resolution and alignment accuracy of the lithography step.

Further, a positive resist like PMMA, where areas unexposed to the e-beam are left on the surface, cannot be used for deposition of several types of molecules in different positions. This is because a polymer area positioned in the first cycle would be exposed to the electron beam during the second exposure cycle and later dissolved during the development.

2.2   Measurement setup

The analysis of the waveguide samples was carried out by using a confocal microscope equipped with two scanners (Olympus FV-1000). The scanners are used to either direct or collect light from a specific, diffraction limited spot on the sample. The scanner motion and location can be controlled by the computer software. In Fig. 2.2 is shown schematics for three different measurement methods used in the analysis. A single scanner imaging was used for general inspection of the samples. In this case the scanner was used to control the position of the excitation laser which was set to scan over the whole sample. The luminescence was collected from the location of excitation, which was then guided to the detectors via band pass filters. The filters are adjusted so that one transmits the reflected laser light and the other detects the fluorescence from the C30 or R6G molecules. The sample image was constructed from the luminescence intensity as a function of the xy-position of the laser. Dual scanner imaging was used for excitation and detection of SPPs. In this case, one scanner was used to control the position of the 405 nm excitation laser, which was set to scan only the region of C30 molecules in a spiral-like fashion. Together the molecules and the laser act as SPP-source having a characteristic spectrum of C30. To image SPPs, a second scanner was used to record the luminescence of the sample as a function of the scanner xy-position. The luminescence signal was guided to the detector via band pass filter adjusted to detect either the C30 or R6G emission. The spectral measurements were made as follows. One scanner was used to control the position of the excitation laser (405 nm). Again, the excitation laser was set to scan only the region of C30 molecules. The luminescence was collected from the specific location of interest (for example the edge of silver stripe or R6G region) on the sample by using the second scanner. The luminescence signal was guided to the detector via a band pass filter whose *spectral position* was scanned through the wavelengths of interest. The spectrum from the location defined by the scanner 2 was constructed by plotting the intensity measured by the detector as a function of the wavelength.

Single scanner

488 nm laser

xy Scanner 1

Band pass filter (λ2) — Detector for λ2

Band pass filter (λ1) — Detector for λ1

Intensity (λ1,x,y)

Intensity (λ2,x,y)

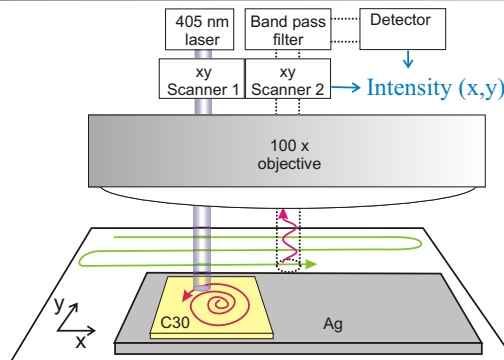100 x objective

y

x

C30   Ag

- One scanner controls the position of the excitation laser (488 nm), which is used to scan the whole sample.

- The luminescence is collected from the same location, which is then guided to the detectors via band pass filters. The filters are adjusted so that one transmits the reflected laser light and the other detects the fluorescence from the molecules (C30 or R6G)

- The images are constructed from the xy-position of the scanner and from the luminescence intensities at each detector.

Dual scanner

405 nm laser

Band pass filter

Detector

xy Scanner 1

xy Scanner 2

Intensity (x,y)

100 x objective

y

x

C30   Ag

- One scanner controls the position of the excitation laser (405 nm). This excitation laser scans only the region of C30 molecules.

- The luminescence is collected from different locations on the sample by controlling the xy-position of the scanner 2. The luminescence signal is guided to the detector via band pass filter adjusted to detect either the C30 or R6G emission.

- The image is constructed from the xy-position of the scanner 2 and from the signal intensity at the detector.

Spectral measurements

Intensity (λ)

405 nm laser

xy Scanner 1

Detector

Adjustable Band pass filter

xy Scanner 2 (stationary)

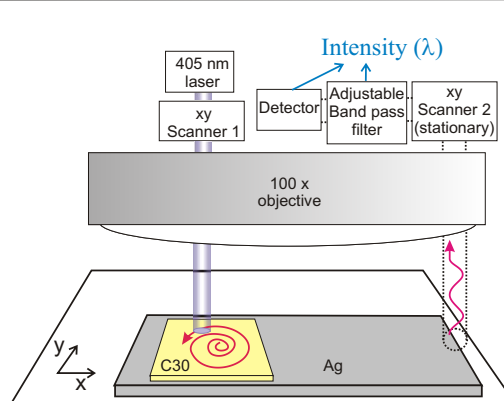100 x objective

y

x

C30   Ag

- One scanner controls the position of the excitation laser (405 nm). This excitation laser scans only the region of C30 molecules.

- The luminescence is collected from the specific (stationary) location of interest on the sample by using the scanner 2. The luminescence signal is guided to the detector via a band pass filter whose spectral position is scanned through the wavelengths of interest.

- The spectrum from the location defined by the scanner 2 is constructed from the wavelength-information of the band pass filter and from the signal intensity at the detector.

FIGURE 2.2 Different measurement schemes using a confocal microscope.

2.3 Molecular coupling between photons and plasmons

2.3.1 Molecular incoupling of waveguided SPPs

The dependence of molecular emission on the distance from the metal surface. First we will show that by varying the distance of the molecular film from the metal surface, the intensity of the fluorescence signal changes. In Fig. 2.3 is shown three cases: a) The molecular film (C30, thickness 50 nm) is deposited directly on top of the Glass/ITO substrate; b) The molecular film (C30) is deposited on top of the silver film; c) A spacer layer (SU-8 polymer film, thickness 40 nm) is deposited in between the C30 and silver film, so as to increase the distance between the two. The R6G area seen on the left of the waveguide is not relevant for the next considerations.
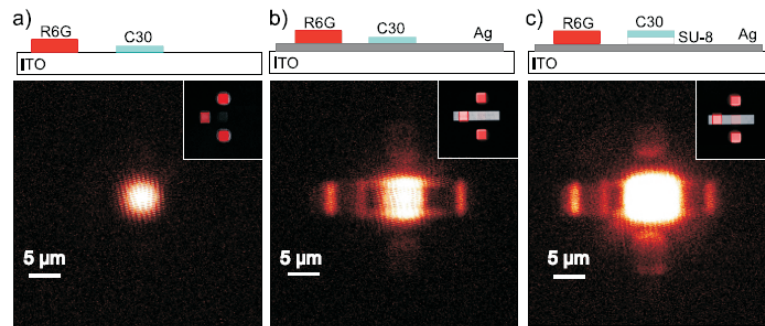

FIGURE 2.3 The effect of the spacer layer between the C30 molecules and the metal on the emission intensity. a) A sample without any metal layer but with C30 region in the center and R6G regions in the three arms. The right arm has no dye. b) Similar to a) but with a plasmonic waveguide added. c) similar to b) but with a spacer layer (40 nm thick) added between the C30 and the metal. Images are taken in dual scanner configuration with one scanner localized only onto the C30 region (excitation with 405 nm laser) and the other scanner set to the detection bandpass of 520-620 nm including both C30 and R6G emissions. In the insets: single scanner confocal images with gray-blue showing the reflection image and red showing the R6G and C30 emission image (488 nm excitation and 520-620 nm bandpass detection).

All the samples were measured under the same excitation and collection conditions. The comparison between the case a) and case b) shows a small increase of the emission intensity from the C30 in the sample b). There are two possibilities for this effect: 1) the silver surface acts as a mirror for both the excitation light and emission light from the molecules. This increases the excitation probability of molecules, and further reflects all the emission to the upper half space. 2) The excitation and fluorescence enhancement in the vicinity of the metal surface have been reported by several authors [71], and this could contribute to the intensity.

However, when a spacer layer is added between the silver and the molecular film, the fluorescence intensity from the C30 area strongly increases (compare the

samples b) and c)). Assuming the excitation rate is not modified, the result implies that other, nonradiative energy transfer mechanisms are present in case b). In particular, these mechanisms can be identified to be the coupling of the radiative dipole to SPPs and lossy waves. Note that the decreased intensity in b) is in qualitative agreement with the discussion in section 1.3, since the coupling to these nonradiative modes (that will not contribute to the photon flux and therefore are not visible in the image) increases when the distance between the radiating dipole and the metal surface is decreased. On the other hand, as seen in case c), adding the spacer layer decreases the coupling to these modes and results in an increase of the photonic emission intensity. The increase of the emission intensity of the C30 molecules from sample a) to sample c), which both have molecules away from the metal surface, can be explained by a mirror effect which increases the excitation of the molecules and the efficiency for collection of the photonic emission.

The results presented above imply that the molecular emission is increasingly coupled to nonradiative modes when the distance between the molecule and the metal surface is decreased. However, results do not provide sufficient information to judge whether the molecular emission is coupled to SPPs or lossy waves.

The luminescence intensity from the end of the silver waveguide depends on the distance from the C30 area. Note also that other parts of the sample in case b) and c), and in particular the right end of the silver stripe, also exhibits luminescence although the excitation light is directed only to the center (C30) area. Next, this emission is shown to originate from the SPPs propagating along the waveguide which are then elastically scattered to photons at the end of the waveguide. As discussed in section 1.1, the surface plasmons are dissipated as heat through ohmic losses in metal. Thus, by varying the distance between the SPP source (C30 area) and the end of the waveguide, the intensity of the photon flux at the end of the waveguide should vary. Further, by assuming that the SPP-to-photon scattering efficiency at the end of the waveguide is independent of the incident SPP intensity, the measured intensity at the end of the waveguide should decay exponentially with increasing distance. To test this, samples with varying length between the C30 area and the waveguide end were fabricated and the distance dependence of the luminescene signal intensity at the end of the waveguide was measured. Several sets of samples were fabricated (i.e., several chips each having many waveguides with varying lengths). As expected for SPPs, the intensity showed exponential dependence on the length with a characteristic propagation length varying from 7 to 10 micrometers between the sets of samples. These values are in reasonable agreement with the values previously reported for plasmon propagation at silver-air interface (20 μm at 514 nm excitation wavelength) [47]. The results from a one set of samples are shown in Fig. 2.4.

Importantly, since our measurement method relies on the intensity of the photon flux incident on the photodetector rather than SPP intensity in the silver stripe, it is essential to distinguish between the two contributions (SPP-originated and free

space photons) to the measured signal. Such an exponential dependence of the intensity is a solid proof that the luminescence at the end of the waveguide originates from the SPPs.
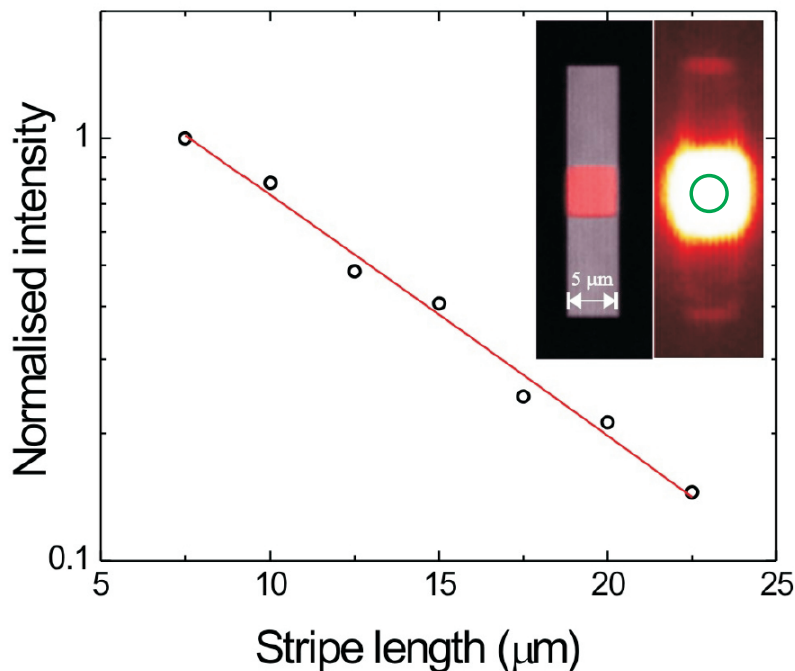

FIGURE 2.4 The luminescence intensity at the end of the stripe as a function of the stripe length (black circles). The red line is a fitted exponential decay yielding a propagation length of 7.7 μm. Inset: Confocal microscope images of one of the measured waveguides taken with the single scanner and the dual scanner setups. The distance between the C30 area and the end of the waveguide is 10 μm. A luminescence signal from elastically scattered SPPs at the end of the waveguide is clearly visible in the dual scanner image (right). Adapted from the paper **I** of this thesis.

The spectrum of the SPPs at the end of the waveguide (or SU-8 edge) corresponds to the emission spectrum of C30. The exponential distance dependence of the luminescence intensity implies that it is due to SPPs that are originated from the excitation area and propagating along the waveguide and then subsequently elastically scattered to photons at the end of the waveguide. However, this does not constitute a proof that the SPPs are originating from the *relaxation of C30 molecules.* It is well known that SPPs can be excited by several mechanisms as discussed in section 1.1. In particular, since the excitation laser light is incident on a silver surface and the SU-8 polymer (host for C30 molecules), it is possible that the defects or impurities at the silver surface or in the polymer host excite the SPPs. To rule out this possibility, spectral measurements for the luminescence at the end of the waveguide were performed. In figure 2.5 is shown the luminescence spectrum from the end of the waveguide together with the emission spectrum measured directly from the C30 area. In both

cases, the excitation light is directed only to the C30 region. As can be seen, the resemblance of the two spectra is high, confirming that the luminescence intensity measured at the end of the waveguide is originating from the C30 molecules. The horizontal shift in the spectra could originate from wavelength dependent propagation losses of SPPs. The short wavelengths are subject to higher losses, which shifts the peak value of the SPP spectrum (red curve) to higher wavelengths.
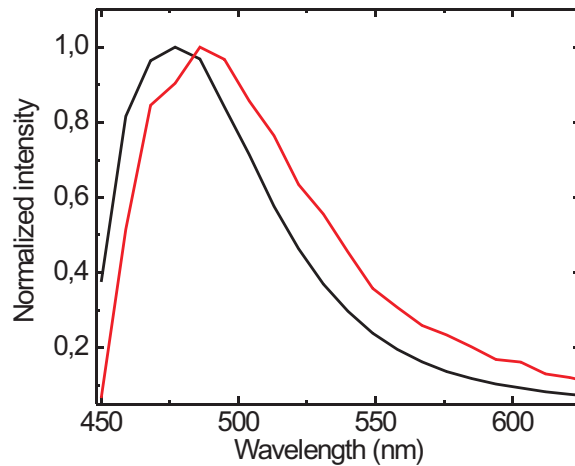

FIGURE 2.5 The luminescence spectrum from the end of the waveguide (red) together with the emission spectrum measured directly from the C30 area (black).

To summarize, the above three measurements state that:
1) The nonradiative decay rate of the excited C30 molecules changes as the distance between the molecular film and the silver surface is varied. For the two distances measured, the fluorescence decreases as the distance is decreased, implying other, nonradiative decay routes for molecules (these could include SPPs or lossy waves).
2) The luminescence intensity measured at the end of the waveguide depends exponentially on the distance r between the C30 area and the end of the stripe. Thus the measured luminescence comes from the SPPs (for free space photons, one expects the intensity to be proportional to $1/r^2$).
3) The luminescence spectrum at the end of the stripe resembles the emission spectrum of the C30 molecules. Thus the SPPs at the end of the waveguide originate from the nonradiative decay of the C30 to SPPs.

Taken together, these results constitute a proof that C30 molecules can be coupled to propagating SPP modes within the waveguide.

2.3.2 Molecular outcoupling of waveguided SPPs

In this section it is shown that the molecules can be used to couple waveguided SPPs to photons. In particular, two different species of molecules are used to realize

a full cycle of photon-SPP-photon conversion, in which the incoupling of the photon is separated by several micrometers from the location of outcoupling. Note that in principle this was already done in previous section, in which the incoupling of photons to SPPs was made by using C30 molecules and the elastic scattering out of the waveguide was used to couple SPPs to photons. The important difference here is that now also the SPP-photon conversion is realized by using molecules. In this case, the outcoupled photon has a different energy than the SPP exciting the molecule: Since the molecular absorption is usually strongly dependent on the energy of the excitation, this enables *a energy (or frequency) dependent SPP-photon conversion*. In the view of plasmonic information technology, this sort of structure could be used for selectively coupling out a certain frequency signal from the SPP waveguide, while the other frequencies would continue their propagation as SPPs. Since organic molecules have been specifically developed for various laser and spectroscopic applications for decades, there exists a wealth of options in terms of absorption and emission wavelength, strength, as well as of vibrational relaxation properties. Thus the approach provides flexibility for designing future plasmonic devices.

In Fig. 2.6a is shown an image of the waveguide structure. The excitation of SPPs is made with a 405 nm laser in area 1, from where the SPPs propagate along the waveguide, reach the area 2 in which the R6G molecules are excited by the SPP. The R6G molecules relax to SPPs or to free space photons, with frequencies characteristic to R6G. The reference areas 3 and 4 are not connected by the waveguide to the SPP source and are used to rule out the possibility that the intensity from the R6G regions originates from the stray light (backround light originating for example from the reflections of the excitation laser or photon emission of the C30) in the setup. As can be seen in Fig. 2.6 b, these areas have negligible intensity, which implies the stray light is not playing a significant role in the excitation of the R6G areas. However, the R6G area on top of the waveguide shows intensive luminescence, in particular at the front and the back edge. Further, both ends of the waveguides show luminescence, which is originating from the elastic scattering of the SPPs to photons.

While the above result implies that the luminescence from the region 2 is due to SPPs, the actual excitation and the emission of R6G has to be verified by measuring the spectral characteristics of the luminescence. For this, the sample structure was modified from the previous one by introducing a second area of SU-8 on the opposite end of the waveguide, *but without R6G* (area 3 in Fig. 2.7b). To rule out the free space photon contribution to the measured luminescence, similar reference areas (as the areas 3 and 4 in Fig. 2.6a) were fabricated (not shown in the figure), and first the plasmon excitation and propagation was verified as previously (2.7a). Further, the spectral characteristics of the luminescence from several areas was measured. By inspection of the spectra measured from the areas c, d and e (Fig. 2.7b) one can verify the molecular outcoupling of SPPs. Consider first the area c (the edge of SU-8 region), where the strongest luminescence signal can be observed at the back
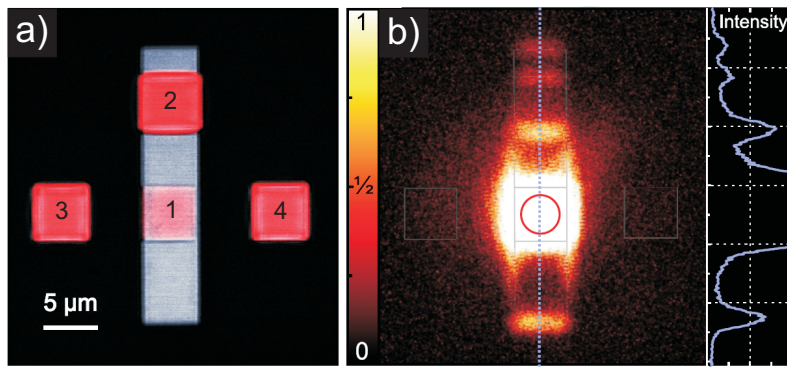
FIGURE 2.6 a) An image taken with a single scanner setup by scanning the sample with the excitation light (488 nm) and simultaneously collecting data in two channels. b) An image taken with a dual scanner setup where the C30 molecules are excited with 405 nm (the red circle corresponds to the area of excitation) and emission with a bandpass of 520-620 nm is collected with a second independent scanner. The contour of the waveguide is overlaid with the intensity map for easy comparison. The intensity profile along the blue dotted line, indicated in the figure, is shown on the right. Adapted from the paper **I** of this thesis.

edge of the region with SU-8 resist (this region similar to the R6G region in the upper arm but without dye molecules). The spectrum of the signal is shown in the inset c of Fig. 2.7b. The resemblance of the spectrum with the spectrum of C30 measured by a direct excitation (shown with a blue line) is evident. The emission shown in the inset c originates from elastically scattered SPPs (the edge of the SU-8 layer acts as a scattering center), which were excited by the C30 molecules. The insets d and e of Fig. 2.7b are taken from the area 2 where the polymer matrix contains R6G molecules. The strongest emission signal appears at the back edge of the rectangular R6G region but some intensity is also observed in the center. In both cases, the spectrum is composed of the spectra of both C30 and R6G as can be seen by comparison with the emission spectra obtained by direct excitation (R6G emission spectum obtained by direct excitation is shown as red). The relative contribution of the R6G is strongest in the spectra measured at the center of the R6G region, but at the edge its contribution is also substantial.

In the center of the R6G (area d), the emission with the C30 spectrum could originate from scattering of SPPs from the imperfections of the polymer area. The remaining interesting questions are what are the mechanisms of the R6G excitation, and R6G emission to the far field. On the right of Fig. 2.7a , the intensity profile of the SPP waveguide is shown along the dashed blue line. Note that the intensity peaks coincide with the discontinuities at the waveguide (the edges of the SU-8 and waveguide). In particular, the center of the R6G region 2 shows significantly less luminescence than the edges. This information can be used to draw conclusions on which of the two competing processes in the R6G region, namely 1) R6G relaxation
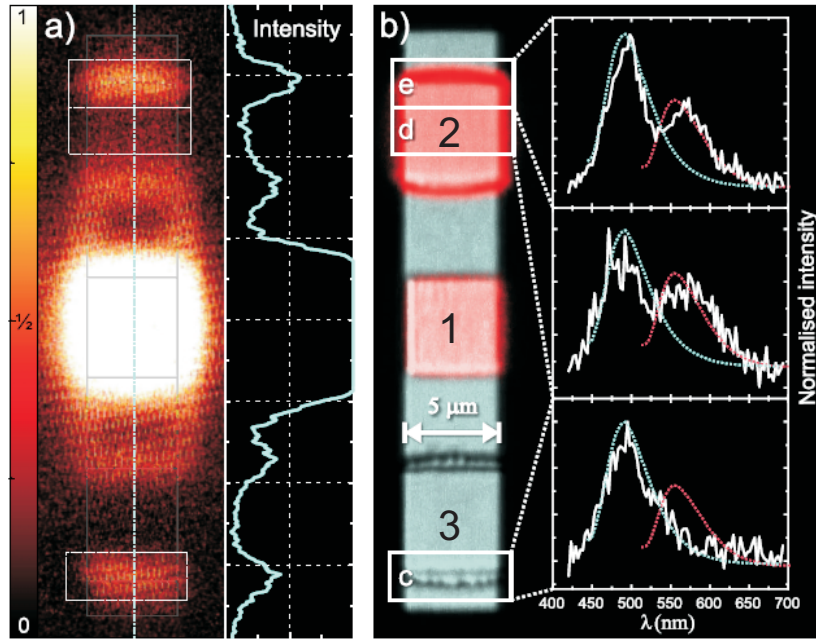
FIGURE 2.7 a) An image obtained by a dual scanner measurement where the excitation was only on the C30 area in the middle and the collection was scanned over the sample, verifying the SPP propagation along the waveguide. The C30 molecules were located in the center of the waveguide (region 1 in b)), and the R6G molecules in the upper arm (region 2 in b)). The SU-8 structure without dye molecules in the lower arm served as a reference (region 3 in b)). The intensity profile along the blue dotted line is shown on the right. b) The spectra measured at different regions under excitation of the C30 with 405 nm laser are shown in the insets c)-e). The reference spectra of the C30 (blue) and R6G (red) measured by direct excitation are shown for comparison. The C30 spectra was observed far away from the excitation region, which is a signature of the C30 excitation decay to SPPs. The spectra from the R6G area has characteristics of both C30 and R6G, which demonstrates a full cycle from photons to SPPs and back to photons by using molecules. Adapted from the paper **I** of this thesis.

to photons and 2) R6G relaxation to SPPs, is dominant. If R6G would decay mainly to photons, one would expect the center region to have comparable intensity with the edges. Hovever, as the majority of the R6G intensity is concentrated at the edge of the SU8 region, it is reasonable to assume that most of the excited R6G molecules decay back to SPPs, which are then elastically scattered to photons from the SU-8 edge. Further, the discussion in section 1.3 implies that the molecules excited by the SPPs are also more likely to decay to SPPs than to photons.

The presented results show that the initial excitation by 405 nm light is coupled to the SPPs via C30 molecules, after which SPPs propagate approximately 10 micrometers and excite the R6G molecules, which then emit either 1) photons or 2) more likely SPPs that are consequently elastically scattered to photons. Thus, a full cycle of molecular photon-SPP-photon coupling, with spatially separated in and

outcoupling locations, is demonstrated.

2.4 Molecular frequency conversion of SPPs

In this section we show that molecules can be used to realize a frequency down-conversion of SPPs. The realization utilizes the vibrational relaxation of organic molecules, which carries away the excess energy related to downconversion. The schematics of the converter is presented in Fig. 2.8.
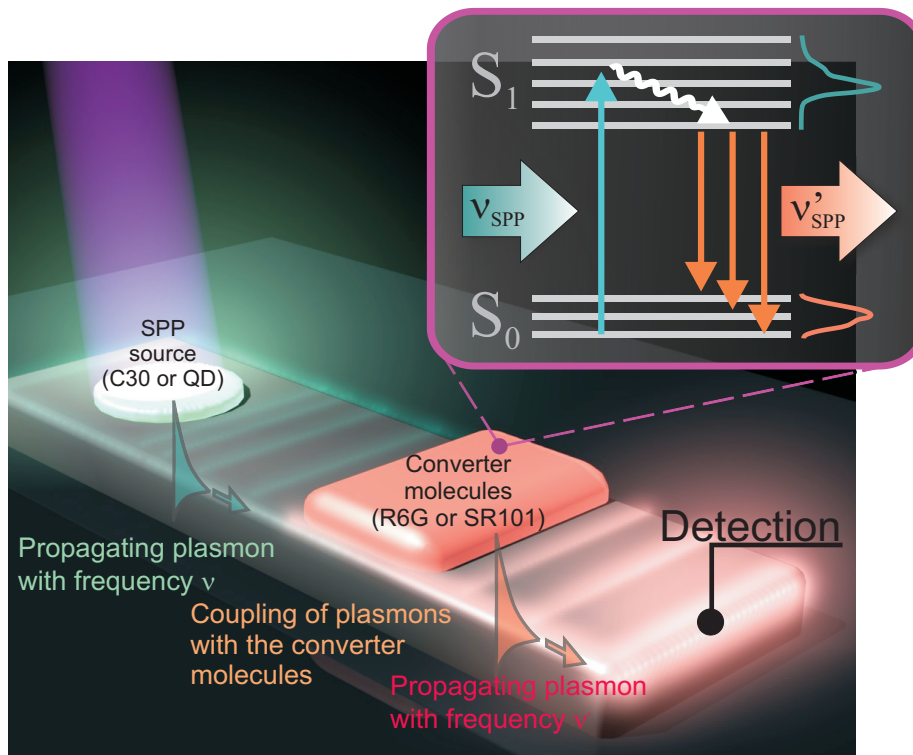

FIGURE 2.8 The schematic presentation of the frequency conversion. The C30 molecules are excited by 405 nm laser excitation, which, by relaxation, emit SPPs into the waveguide with frequency ν which is characteristic to C30 emission. The SPPs propagate along the waveguide and consequently enter the area where the waveguide is covered by the R6G molecules. The R6G molecules are excited from S0 to S1 state by the SPPs. The excitation then relaxes to the bottom of the S1 band by vibrational relaxation. The transition back to S0 state is accompanied by the emission of SPP, but now with different frequency ν' which is characteristic to the R6G emission. The detection of SPPs with the new frequency is made by measuring the luminescence spectrum at the end of the waveguide. Here, the elastic scattering of the SPPs to photons is utilized, which does not change the SPP frequency. Also experiments with another SPP source and converter molecules were made. In this case the SPP source consisted of semiconductor nanocrystals (quantum dots, QDs) and the converter molecules were Sulforhodamine 101 (SR101). Adapted with permission from the paper **II** of this thesis.

Note that since the SPPs are strongly polarized, the coupling between SPPs and molecules depends on the orientation of the molecular dipole moment. Consequently, it is reasonable to assume that the molecules that are excited by SPPs, are more likely to relax to SPPs than to photons. Also the results in the previous section implied that the R6G molecules relax to SPPs which consequently scatter elastically to photons. However, to confirm the SPP emission of R6G, particular care has to be taken to rule out the other possible processes that could result to the presence of R6G luminescence spectrum at the end of the waveguide. These processes are presented in detail in Fig. 2.9.
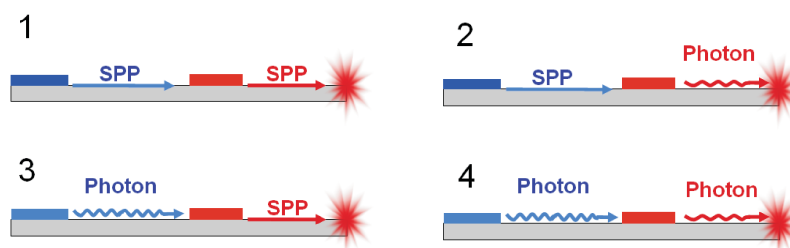

FIGURE 2.9 The possible processes that could contribute to the R6G luminescence spectrum at the end of the waveguide. The SPP source is presented in blue and the conversion molecules as red. The conversion signal is measured at the end of the waveguide. The processes 2, 3 and 4 that include photon contributions, can be distinguished from the process 1 (the actual SPP frequency conversion) by utilizing specially designed reference points on the sample.

The processes 2, 3 and 4 include photon contributions, and may contribute to the luminescence spectrum measured at the end of the waveguide. These processes can be distinguished from the actual SPP frequency conversion (process 1) by designing reference points on the sample that allow one to quantify their contribution to overall luminescence spectrum. In Fig. 2.10a is shown the sample structure along with the used reference points. The point A is used to measure the frequency conversion, whereas B, and D are used to rule out the other processes. The point E and C are used to quantify the incident SPP intensity at the distance where the R6G region begins (i.e., the SPP intensity incident to the conversion region). Note that the sample is designed in such a way that the points A, B and D (and the points C, E and the front edges of the R6G region) are within the same distance from the SPP source. Since the SPPs propagate to all directions from the source, these points allow to quantify the relative contribution of the different processes. As can be seen from Fig. 2.10b , the point D does not exhibit any luminescence, which rules out the contribution of the processes 3 and 4 to the luminescence at the point A. Further, the point B can be used to quantify the contribution of the process 2 at the point A. The spectra measured at the point A and B are shown in Fig. 2.11a, along with the C30 and R6G spectra measured by direct excitation of the molecular films.
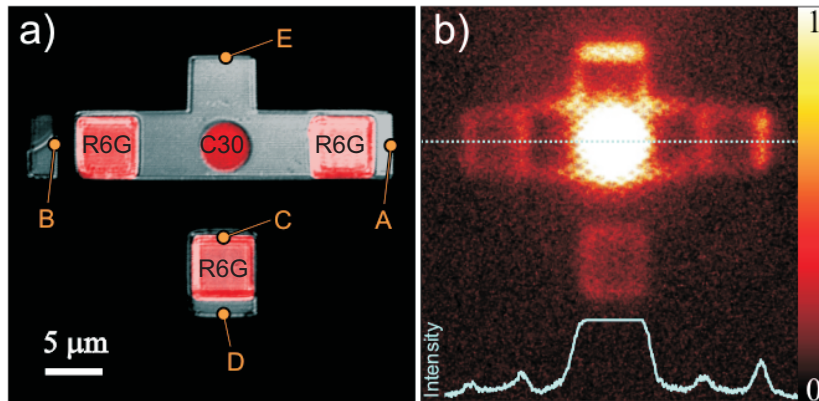
FIGURE 2.10 a) The sample structure used to verify the SPP frequency conversion. The luminescence spectra are measured at the points A, B, C, D and E to distinguish the process 1 from the processes 2, 3 and 4 and to quantify the conversion efficiency. b) A dual scanner confocal microscope image of the experiment where the SPPs are excited. Adapted with permission from the paper **II** of this thesis.

In Fig. 2.11b, the spectrum of the point B is subtracted from the spectrum of the point A, which gives an estimate of the overall frequency conversion efficiency of the structure, yielding approximately 50%. Note that also the point B can contain luminescence intensity from the SPPs that are first converted to R6G frequency, but are then elastically scattered to photons from the end of the waveguide. Part of these photons can be reflected via the point B to the photodetector, thus contributing to the overall intensity measure at the point B. Thus the presented analysis for conversion efficiency is not precise, but rather a minimum estimated value for the conversion. The points E and C can be used to estimate the incident SPP intensity at the front edge of the R6G region, by subtracting the spectrum of the point C (photon contribution) from the spectrum of the point E. By comparing this intensity to the SPP intensity at the point A yields an approximate efficiency of 5% for the device. This low efficiency comes from the high scattering intensity at the edges of the SU-8.

Frequency conversion was also tested for samples that consisted of quantum dots as the SPP source and Sulforhodamine 101 (SR101) dye as a converter. QDs are more stable with respect to bleaching. The bleaching time of QDs was observed to be over an order of magnitude longer than that of C30. The QDs (Invitrogen, Qdot 565 ITK amino) and SR101 have the emission maxima at 550 nm and 600 nm, respectively. Similar analysis as above yielded 15% conversion (see Fig. 2.12). The lower conversion efficiency is probably due to the smaller overlap between the QD emission and the SR101 absorption. Semiconducting quantum dots could have interesting applications in plasmonics. Due to the broad absorption of QD, one could think about building plasmonic device that would convert of a large band into a single frequency. This is complementary to molecules that typically convert one narrow band into another.

34
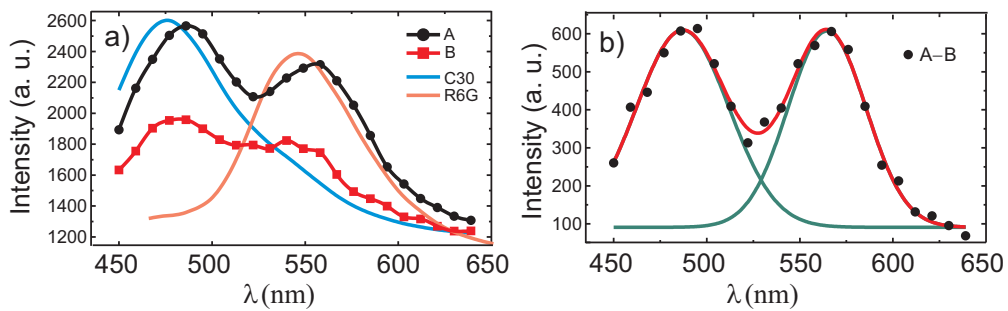
FIGURE 2.11 a) The spectra measured at the point A and B along with the C30 and R6G luminescence spectra measured by direct excitation of the molecular films. b) The spectrum of point B subtracted from the spectrum of point A, giving an estimate of the overall frequency conversion efficiency. Adapted with permission from the paper **II** of this thesis.
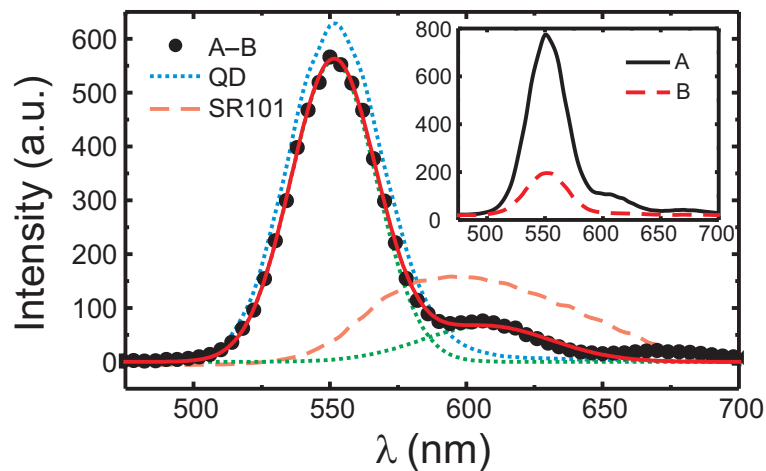
FIGURE 2.12 Frequency conversion for QD-SR101 pair. *SPP spectrum* of the point A (black circles), i.e., the luminescence spectrum of the point B subtracted from the spectrum of the point A. The red line is a fit to the data as a sum of two Gaussian peaks (green dotted lines) corresponding to the emissions of QD (565 nm) and SR101 (600 nm). Blue dotted and red dashed lines are the emissions of pure QD and SR101, respectively. Inset shows the spectra recorded from A (black solid) and B (red dashed). Adapted with permission from the paper **II** of this thesis.

Chapter 3

SPP-molecule interactions in the strong coupling regime

3.1 Rabi split and oscillations

According to the Fermi's Golden Rule, the rate of spontaneous emission is proportional to the optical density of states at the spatial position of the emitter. Thus, any modification in the optical environment of the emitter is bound to affect its optical properties. In particular, the radiative lifetime can either be extended or reduced with respect to its lifetime in vacuum [35]. This phenomenon is also known as Purcell effect and is irreversible; the energy of the photon cannot be transferred back to the emitter [64]. This regime is also referred to as weak coupling regime. In contrast, if the coupling between the photon and the emitter is strong enough, a quasi-lossless strong coupling regime is achieved, in which the energy oscillates coherently between the emitter and the photon, leading to so-called Rabi-oscillations. The resultant system can no longer be described by the uncoupled photon and the emitter, but rather as a superposition of the two. The coupled system energies are modified from the uncoupled case and exhibit an energy gap at a resonance energy, manifested as an anticrossing of the dispersions (also known as Rabi splitting).

While the majority of the recent studies of strong coupling have been made in organic and inorganic microcavities, many of the phenomena in SPP-molecule systems are analogous to these, allowing us to adopt experimental methods and gain qualitative insight by comparing the two systems. Often it is enough to simply replace the cavity photon field by the SPP field. Following a treatment used in [5], in a picture of coupled oscillators the energies of the strongly coupled modes at resonance are given by

$$E = E_0 - i(\gamma_{SPP} + \gamma_X)/4 \pm \sqrt{g^2 - (\gamma_{SPP} - \gamma_X)^2/16}. \qquad (3.1)$$

Here E_0 is both the energy of the SPP and of the molecular transition at resonance,

γ_{SPP} and γ_X are the full width at half maximum linewidths of the SPP and the exciton, respectively, and g is the SPP-exciton coupling strength which depends on the effective oscillator strength f of the exciton and the mode volume V_m as

$$g \propto \sqrt{f/V_m}. \tag{3.2}$$

Without the damping terms γ_{SPP} and γ_X, the equation 3.1 is obtained by finding the system eigen-energies simply by diagonalizing the Hamiltonian at resonance

$$H = \begin{bmatrix} E_0 & g \\ g & E_0 \end{bmatrix}. \tag{3.3}$$

Including damping (the widths γ_{SPP} and γ_X) into the calculation is more complicated and we refer to [5]. The complex energy in 3.1 describes simple exponential damping of the wave function of the system: $\exp(-iEt)$ will now include the damping term $\exp(-(\gamma_{SPP} + \gamma_X)t)$. Note that in addition to this, the damping also affects the Rabi splitting, which is the difference of the new eigen-energies

$$\Delta = 2\sqrt{g^2 - (\gamma_{SPP} - \gamma_X)^2/16}. \tag{3.4}$$

In case of organic semiconductor dye molecules, the oscillator strength can be conveniently controlled by a dye concentration. Note also that the inverse of γ_{SPP} essentially gives the SPP lifetime through the energy-time uncertainty principle, and that this lifetime can be affected through dissipation: By increasing the SPP dissipation, one increases γ_{SPP} and decreases the corresponding lifetime.

3.2 Previous work

Although coherent light-matter interaction has been a topic for intense research in atomic physics communities for decades, the broad attention for such phenomena in the solid state community was caught quite recently. The first observation of strong coupling in inorganic microcavities was reported by Weisbuch *et al.* in 1992 [78] for GaAs quantum wells positioned between two distributed Bragg reflectors (DBR), showing a few meV Rabi split at 5-77 K temperatures. The rather small value of splitting comes from the inorganic cavity oscillator strength, which in this case was $f = 4 \times 10^{12}$ cm^{-2}.

Lidzey *et al.* demonstrated the first strong coupling experiments at room temperature for organic microcavities having a DBR and a silver surface as mirrors [52]. Although large oscillator strengths are a characteristic feature of organic semiconductors, the authors identified two major obstacles for achieving strong coupling in these materials. The large exciton linewidths that result from the inhomogeneous broadening and the presence of a vibronic progression make the strong coupling difficult to observe. To overcome the problem, they used tetra-(2,6-t-butyl)phenol-

porphyrin zinc molecules having a particularly narrow absorption linewidth. The splitting of 160 meV at room temperature, which was an order of magnitude higher than the largest splitting reported for inorganic microcavities, was attributed to the large oscillator strength $f = 2 \times 10^{15}$ cm^{-2} of the molecular film. Later, the same group demonstrated strong coupling for a different class of molecules as well, namely J-aggregates [53].

Bellessa *et al.* demonstrated Rabi splitting for SPPs and J-aggregates positioned on top of the metal surface supporting SPPs [9]. Interestingly, no cavity is needed for observing the strong coupling between the SPPs and J-aggregates. This is due to the intrinsic field enhancement of the SPP near the metal surface. This may prove useful from the application point of view, since in the case of SPPs, the structure is very easy to fabricate. Further, it would be interesting to know whether the possible SPP excitation onto the silver surface used in the microcavity experiments had any effect on the observed results. Hobson *et al.* [34] studied silver-DBR and silver-silver microcavities, and showed that by replacing the DBR by a layer of silver, the splitting increased. However, this effect was attributed to the decreased mode volume rather than to SPPs.

3.3 Strong coupling between Rhodamine 6G and SPPs

3.3.1 Experimental setup

The samples consisted of a thin layer of silver (50 nm, electron-beam evaporated in ultra high vacuum) on a glass substrate. R6G in four different concentrations was diluted in SU-8 negative resist (Microchem SU-8 2000 series), and then spun cast on top of the silver layer to form approximately 50 nm thick layers. Also reference samples without silver layer were fabricated.

In Fig. 3.1 is shown the schematics of the measurement setup. For excitation of SPPs, a white light source and a hemicylindrical prism in Kretschmann configuration was used (see Fig. 3.1 a). The white light was collimated and aligned by using two adjustable slits. The polarization of the incoming light was adjusted by a rotatable polarizer. Since only the p-polarized light couples to SPPs [81], the possibility to use also s-polarization provides a useful reference when studying the SPP related effects in such configuration. The incident angle of the incoming light was adjusted by a rotatable prism mount. The in-plane wavevector (i.e., the component that is parallel to the sample surface) of the incoming light on a given frequency can be tuned with the incident angle α. The incoming light couples to SPPs on a Ag/R6G interface, when the SPP wavevector equals the in-plane wavevector of the incident light, i.e.,

$$k_{SPP} = \frac{\omega}{c} \sqrt{\epsilon_{substrate}} \sin \alpha, \qquad (3.5)$$

39

where ω is the angular frequency of the light (and the incoupled SPP), c the speed of light and $\epsilon_{substrate}$ the dielectric constant of the substrate and the prism.

The incoupled energies are shown as dips in the reflected light spectrum, see Fig. 3.1 b, detection 1 (DM1). Thus by measuring the dips in spectra for a range of angles, one is able to map out the dispersion curve for the *incoupled* energies of the system. This well established method for measuring the dispersion was first introduced in [37].
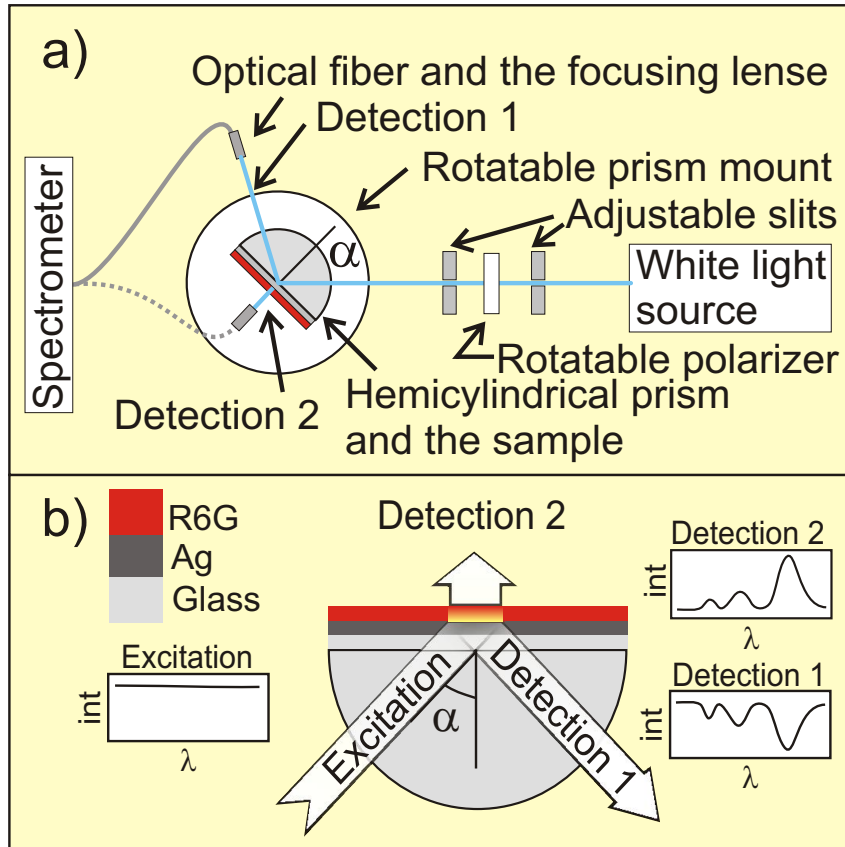
FIGURE 3.1 The measurement setup. a) A white light source and a hemicylindrical prism in Kretschmann configuration was used to excite SPPs. The white light was collimated and aligned by using two adjustable slits. The polarization and the incoming angle of the excitation light was adjusted by a rotatable polarizer and a rotatable prism mount, respectively. b) Two different detection methods, detection 1 (DM1) and detection 2 (DM2), were used to analyze the samples. The part b) adapted with permission from the paper **III** of this thesis.

In addition to the DM1, we use another method (detection 2, DM2) to measure the spectra from the molecule side of the sample. Due to the SPP sensitivity to interface conditions, they are easily scattered to photons from corrugations in a silver surface or impurities in the molecular film and are thus visible in DM2. The method is complementary to DM1 in a sense that it measures the energies of the modes that

are *coupled out* of the system by scattering processes. Later we will show that DM2 in conjunction with DM1 provides us information of the time evolution of the studied system. Note that DM2 has not been used in the previous studies of SPP-organic molecule systems.

In Fig. 3.2 are shown the dispersions measured with both DM1 and DM2 from a sample having only a silver thin film deposited onto the glass substrate. The overlap of the two dispersions verifies that DM2 indeed detects the initially incoupled modes that are consequently scattered to photons. Further, the possible wavelength dependency of the SPP scattering to photons does not significantly alter the dispersions. The slight variation of the two curves on high energies might originate from the SPP losses that are energy dependent: The DM2 measures the SPP modes that have been interacting longer with the system (as compared to DM1) and are thus subject to increased losses; since the SPP losses increase with increasing energy, the measured spectra in DM2 might exhibit a red shift, which in turn shows up as lower energy in the dispersion.
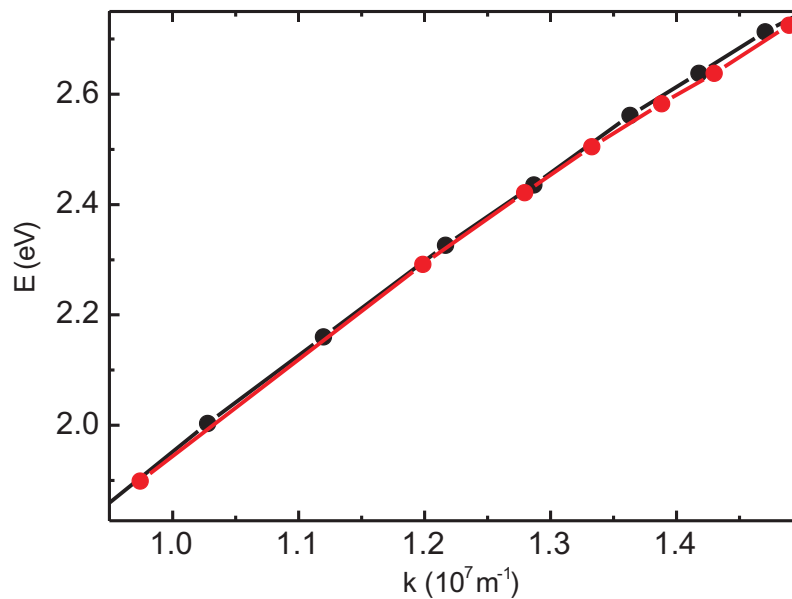

FIGURE 3.2 The dispersion relations measured with both DM1 (black) and DM2 (red) from a sample having only a silver thin film.

3.3.2 Observation of strong coupling and vacuum Rabi splitting; Detection 1

In Fig. 3.3 are shown the measured dispersions with DM1 for thin film silver/R6G samples having four different R6G concentrations (4, 25, 50 and 200 mM) together

with the measured absorption of R6G from the 200 mM reference sample having no silver. For all the samples, the R6G layer was approximately 50 nm thick. As can be seen, the R6G absorption has a maximum and a "shoulder". To deduce the energies of the absorption maximum and the shoulder, two gaussian curves were fitted into the absorption curve. The center points of these two gaussians are plotted as gray horizontal lines.
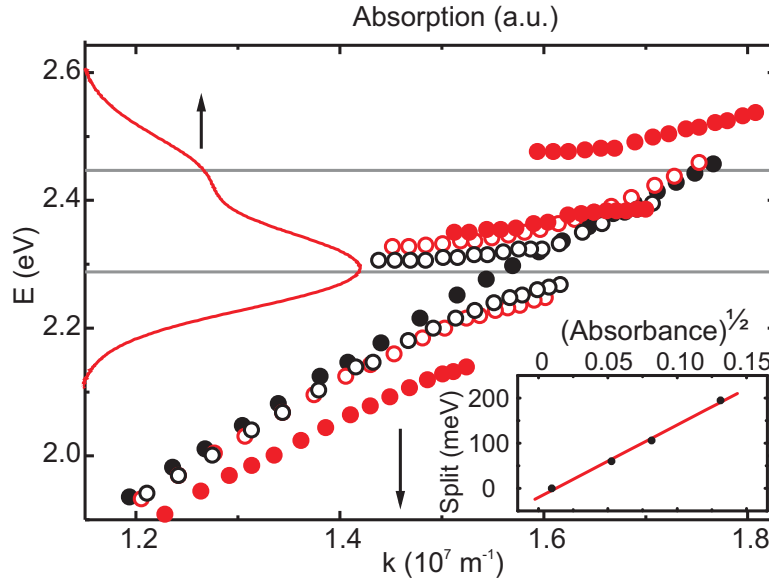

FIGURE 3.3 The dispersions measured with DM1 for samples having different R6G concentrarions: 4 mM (solid black circles), 25 mM (empty black circles), 50 mM (empty red circles) and 200 mM (solid red circles). The solid red curve is the measured absorbance of the 200 mM SU-8/R6G film, and solid grey lines are the absorption maximum and absorption shoulder energies. The inset shows the low energy split as a function of (absorbance)$^{1/2}$ with a linear fit. Adopted with permission from the paper **III** of this thesis.

For the lowest 4 mM concentration, the dispersion resembles that of the theoretically calculated SPP in an Ag/SU-8/air structure. By increasing the R6G concentration to 25 mM, a split appears to the dispersion at the energy corresponding to the absorption maximum of the R6G. This anticrossing behaviour of the dispersion is a manifestation of the strong coupling: There is no mode at the resonance energy E_0 of the uncoupled modes, see Eq. 3.1. This also means that there is no absorption at the energy corresponding to the R6G absorption maximum. By further increasing the concentration of the R6G to 50 mM, the split widens. Furthermore, when the concentration is increased to 200 mM, the split again widens, and a *second* split appears to the dispersion at the energy corresponding to the absorption shoulder.

Let us first discuss the effect of concentration to the amount of splitting. Eqs. 3.1 and 3.2 show that the energy splitting should scale with the square root of oscillator strength. In our case, it is the molecules that oscillate within the electric field

of the SPP. The higher the number of molecules, the bigger is the splitting. This provides a convenient way to control the strong coupling characteristics in organic semiconductor materials. In the inset of Fig. 3.3 is shown the lower energy splitting for the above samples as a function of the square root of absorbance measured from the reference sample having no silver. In agreement with the theory [70], the linear dependency is evident. The observation of Rabi splitting dependency on R6G concentration has the following implication. The molecules are interacting with the SPP *coherently*, that is, the SPP induced polarization of each molecule is in phase with the neighbouring molecules. The ensemble of molecules thus acts as if there was a one single, high strength oscillator.

In general, Rabi splitting in semiconductor cavities can be divided into two categories depending on whether the energy split varies with excitation light intensity or not. The first case is related to high excitation intensities so that the average photon number in a cavity at each instant well above one. Thus each photon entering the cavity increases the total electric field, resulting in a stronger light-matter coupling and increased splitting. In the second case, the excitation intensity is very low such that the average photon number in a cavity is $\ll 1$. In this case (the so-called vacuum field Rabi splitting (VRS)), the cavity is empty of photons or holds only one photon. Consequently, the coherent interaction takes place between only one photon and the molecular ensemble and the power variation of the excitation light does not increase the splitting energy due to quantization of the light field.

In our experiments the excitation light intensity was varied between 0.17-13 W/m^2 (power measured over the visible range), with no detectable effect on the dispersion, which implies that our experiments are made in the vacuum Rabi splitting regime. Note that such independence of the split energy on intensity necessarily implies either 1) the quantization of the field used to excite the system, or 2) the quantization of the field of the system itself, or 3) both. This is because in the case of classical electromagnetic field, the electric field intensity and the Rabi splitting of the system should scale with the excitation intensity even in the low intensity regime. Further, this is so-called *many-atom* vacuum Rabi splitting, since there are several molecules contributing to the overall oscillator strength, but only one photon.

3.3.3   The effect of the interaction time; Detection 2

The same samples were measured with DM2 as well, yielding the dispersions shown in Fig. 3.4. For the DM2, we expect that the signal comes from the scattered strongly coupled modes of the system. While the dispersions with DM2 resemble those of DM1, there are deviations that require further explanation. DM2 shows an additional emission branch nearly independent of the in-plane k vector at around 2.17 eV, for the 25 and 50 mM samples. According to the measurements of a reference sample having R6G film but no silver, this branch could be identified as the spontaneous, non-coupled, emission maximum of R6G. This behaviour is reported also for

J-aggregates [9,34]. More importantly, for each sample DM2 shows a larger splitting if compared to DM1. Particularly distinctive is the difference for the 50 mM sample, in which the upper energy splitting in not visible at all for DM1, but shows up when using DM2 (this also applies for the lower energy split in 4 mM sample). Note that the excitation (incoupling) of the system is exactly the same for both detection methods. Thus the difference between the two must originate from the events taking place after the incoupling. Therefore, by utilizing DM2 in conjunction with DM1, one gains information of the system dynamics.
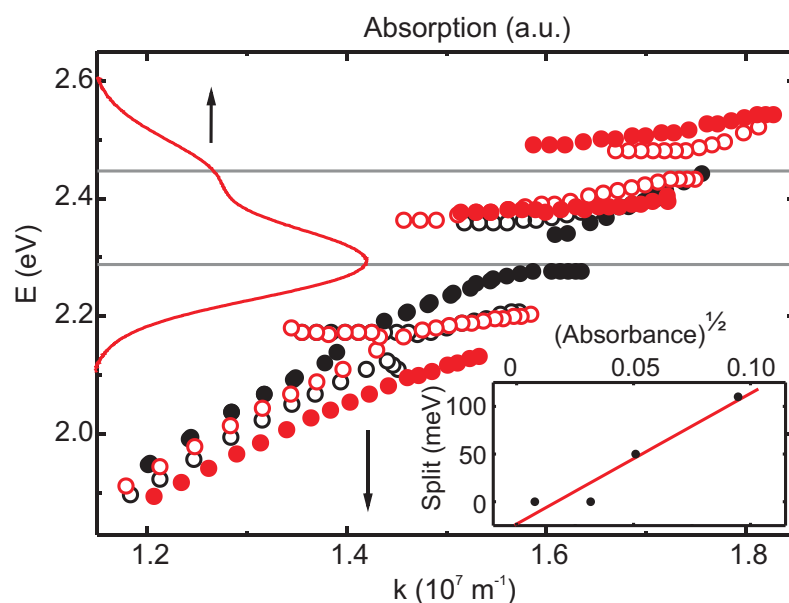
FIGURE 3.4 The dispersions measured with DM2 for samples having different R6G concentrations: 4 mM (solid black circles), 25 mM (empty black circles), 50 mM (empty red circles) and 200 mM (solid red circles). The solid red curve is a measured absorbance of the 200 mM SU- 8/R6G film, and solid grey lines are the absorption maximum and absorption shoulder energies. The inset shows the high energy split as a function of (absorbance)$^{1/2}$ with a linear fit. Adopted with permission from the paper **III** of this thesis.

To gain better insight to the differences between the two detection methods, one needs to examine the details of the in- and outcoupling of the hybrid modes. In Fig. 3.5 is shown a schematic of the system under study. The incoupling is via near-field component of the incident photon: the timescale of the event cannot exceed the time the photon spends in the immediate vicinity of the surface. After this time, there is no possibility for the strongly coupled system to affect the signal measured by DM1.

In contrast, for DM2, the interaction time of SPPs with the molecular film is only limited by the dissipation or scattering of the SPPs. In addition to above, somewhat geometrical consideration, the analogies found in microcavities further justify

the assumption that the interaction time indeed plays a role in our system as well. The Rabi splitting in microcavities can be controlled by adjusting the Q-factor, since it essentially defines the lifetime of the cavity photon, that is, the interaction time between the photon and the optically active material within the cavity [65].
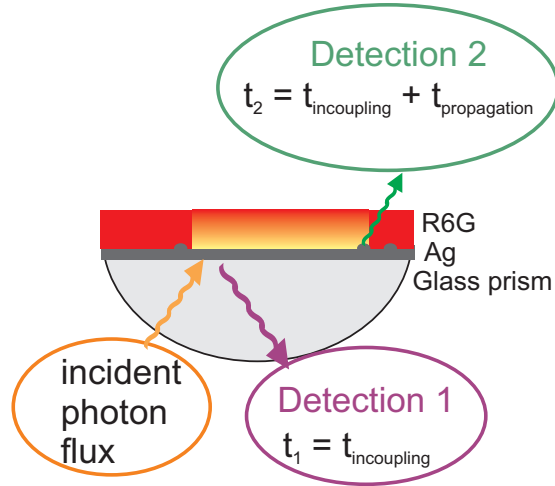

FIGURE 3.5 The difference between DM1 and DM2 comes from the differences in the interaction times. In DM1, the incident photon interacts with the system via its near-field component, and thus the interaction time is limited to the time the photon spends in the immediate vicinity of the silver surface. In DM2, however, the interaction time is limited only by the scattering (or dissipation) of the SPP mode.

Since the scattering centers are randomly distributed over the sample, the propagation length (and the interaction time) of the polariton prior to the scattering is random as well. Thus, in thin film samples, as studied by DM1 and DM2, the interaction time cannot be precisely controlled, but rather has some distribution which depends on the defect density of our samples. Since the interaction time plays a central role in strong coupling dynamics, it is of interest to gain control over such a parameter.

For this purpose, we introduced a completely different technique to study the SPP-molecule strong coupling: we fabricated waveguide samples with well defined R6G molecular areas at chosen places; the R6G area length was easily controlled by standard e-beam lithography methods. In these samples, the SPP is launched to the waveguide at place spatially separated from the R6G interaction area. The SPP then propagates to the R6G area. Now the SPP-molecule interaction starts at the front end of the R6G/polymer area (this is to some extent analogous to the incoupling event in DM1 and DM2), and the outcoupling into radiation to be detected takes place in the back end (due to polariton scattering from the R6G/polymer edge). By varying the length of the R6G area, the propagation distance of the hybrid polariton (and thus the interaction time between R6G and SPP), could be adjusted.

45

In Fig. 3.6 is shown a schematic of such a technique. Note that the defect density does not anymore define the interaction time, since by local spectral measurements we are able to analyse only the modes that are propagated to the very end of the R6G area. Thus, by this method one can conveniently remove the undesired randomness from the interaction time present in the thin film samples. Since the interaction time is now determined by the mode propagation speed and the length of the R6G region, we can make an estimate of how precisely this interaction time can be controlled. The length of the R6G area can be controlled by standard lithography methods within 10 nm accuracy. Approximating the mode propagates at half the speed of light (see the slope of the dispersions), one gets the minimum resolution for the control of interaction time $\Delta t_{interaction}$ = 0.06 fs, well below 10 fs timescales that are relevant to SPP dephasing [55].
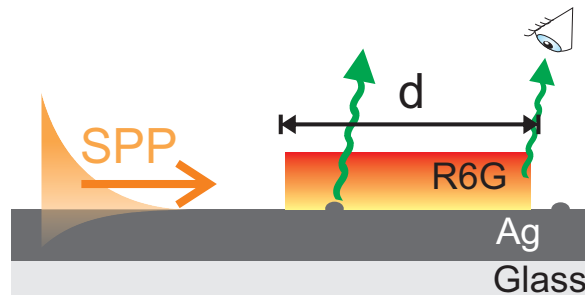

FIGURE 3.6 The interaction time can be controlled by introducing a waveguide sample with well controlled R6G area of length d. Note that the modes that are scattered due to a defect in the waveguide do not contibute to the spectra since they are measured locally from the very end of the R6G region. Thus the defect density of the sample does not affect the interaction time for the recorded photons.

The measurement setup poses some restrictions to the length of the R6G region: If the region is very short (say, below 500 nm in length) the SPP scattering in the *front* end might contribute to the measured spectra from the backend due to finite (diffraction limited) size of the detection spot. Further, if the R6G area exceeds a certain length (10 μm), the signal at the backend starts to be very small due to the SPP losses. In future, this problem could be partially circumvented by introducing a higher power and nonbleaching source which would allow for higher intensities and signal averaging times.

Consequently, the concentration for R6G was chosen in such a way that within the limits of the possible R6G lengths, as wide range of strong coupling phenomena as possible, could be covered. We fabricated samples with three different lengths of R6G, 1 μm, 2 μm and 5 μm. As the SPP source we used Coumarine 30 (C30) molecules (embedded in SU-8) deposited on top of the waveguide in a location separated a few microns from the R6G area. The C30 molecules, having an emission maximum around 2.55 eV, were excited with a 405 nm laser. The fabrication of such

waveguide samples as well as details of the experiment are described in chapter 2. The spectra measured from such samples together with the dispersions measured from the thin film samples (DM2) with different concentrations of R6G are shown in Fig. 3.7.
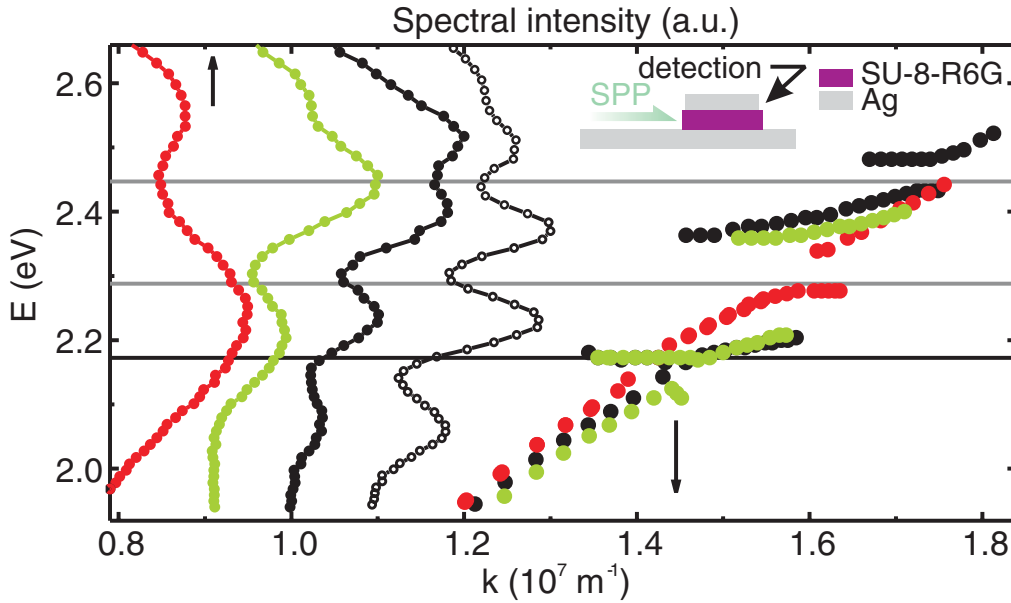

FIGURE 3.7 The luminescence spectra measured from the waveguide samples having different lengths of R6G deposited on top of a waveguide (see the inset schematic), along with the dispersion curves of the thin film samples measured with DM2. For a short 1 μm R6G area (red curve), the spectrum has two peaks that can be identified to be the C30 (2.55 eV) and R6G (2.25 eV) emissions (compare with the 4 mM dispersion curve (red) having a very small split). For the 2 μm sample (green), a clear dip in the luminescence spectrum is seen around the main absorption of R6G (2.29 eV) which coincides in energy with the split in the dispersion curve of the 25 mM sample (green). For 5 μm sample (black), also the second split at the absorption shoulder energy appears to the luminescence spectrum (compare with the dispersion curve of 50 mM sample having two splits (black)). The spectrum plotted in black empty circles is measured from a waveguide sample having a 5 μm R6G area as well, but with a layer of silver deposited on top this area (as in the schematic). Note that the same color is used for pointing out the cases when the dips in the spectra and the splits in the dispersions appear at the same energies. The black horizontal line is the measured R6G emission and the gray lines absorption maximum and absorption shoulder energies. Adopted with permission from the paper **III** of this thesis.

For the 1 μm sample, the luminescence spectrum shows only two peaks, one at around 2.55 eV and the other at 2.25 eV. These peaks can be identified to be the C30 and the R6G spontaneous emission peaks, respectively. The result is similar to the one shown in the previous chapter of this thesis. Here, the C30 originated SPPs enter the R6G region, part of them excite the R6G molecules, which by spontaneous

emission emit another SPP with another frequency. These SPPs are scattered to photons from the end of the R6G region, yielding a spectrum having two peaks that correspond to R6G and C30 emission maxima. Since the luminescence spectrum of the waveguide sample shows normal spontaneous emission from the R6G, we expect that the SPP-R6G interaction is in the weak coupling regime. By comparing this spectrum with the 4 mM thin film sample dispersion, having a very small or no split, we can draw analogies between the two results; In thin film samples the low R6G concentration (low number of oscillators), is not sufficient to result in strong coupling between R6G and SPP. Similarly, the short R6G area in waveguide samples yield a short interaction time between the SPP and the molecules, resulting in spectral features characteristic for weak coupling regime.

By increasing the R6G area length to 2 μm, a *dip* appears in the luminescence spetrum at around 2.3 eV. This effect is comparable to the Rabi split at the same energy present in thin film samples when the concentration is increased to 25 mM. Note that in thin film samples the angle resolved reflection spectroscopy allows the mapping of k-vector dependent energies of the system. In contrast, for waveguide samples, there is a broad SPP k-vector distribution (originating from C30) incident to the acceptor area. Consequently, the measured luminescence spectrum does not give access to the k-vector dependencies of the system energies. Rather, the signature of Rabi split in the luminescence spectrum is seen as a dip at the split energy.

By further increasing the R6G area length to 5 μm, a second dip appears in the luminescence spectrum at around 2.45 eV. This dip corresponds to the second Rabi split in the dispersion for the 50 mM sample originating from the R6G absorption shoulder. Apart from the interaction area length, we increased the SPP-matter interaction by also fabricating a layer of silver on top of the interaction area, thereby blocking the decay into radiative modes. With such a sample, the strong coupling features become very prominent (see the spectrum plotted as empty black circles in Fig. 3.7)

Recently, another method for ultra-fast control over the strong coupling was introduced, in which a three level system and a femtosecond control pulse was used [29]. The authors reported strong coupling control in sub-Rabi cycle timescales, gaining access to a class of extremely nonadiabatic phenomena. Their method forms a promising new platform to study novel sub-cycle QED effects. It would be of interest to consider the possible analogies between their method and the waveguide based method reported here. Certainly the active control of strong coupling over such timescales is extremely appealing. However, our waveguide-based method provides extremely simple method for similar control, and potentially in much shorter timescales (10 fs control pulse in [29] vs. 0.06 fs control over the interaction time in our case).

It is interesting and somewhat counterintuitive to note that although only two species of molecules are present, the luminescence spectra for 2 μm and 5 μm sam-

ples exhibit several peaks, having virtually no resemblance to the normal emission spectra of either of the molecules. The above experiments verify that one can tune the strong coupling characteristics of the SPP-R6G system by simple means of stardard electron beam lithography. From the application point of view it is notable that both the resist used, and the relevant dimensions of the system are directly applicable to photolithoraphy based fabrication of such structures.

3.3.4 SPP mediated hybridization of the molecular excitations

Then let us discuss the *second* split in the dispersions. Lidzey *et al.* reported similar behaviour for semiconductor microcavities, in which two different semiconductor dyes were positioned into the cavity [51]. The dyes were spatially separated to rule out the dipole-dipole interaction. The resulting dispersion exhibited two anticrossings at the energies corresponding to the absorption maxima of the two dyes. The center branch thus was a superposition (hybrid) of the three uncoupled eigenstates (cavity photon and the two excitons). The authors concluded that it was the cavity photon that induced the hybrization of the two spatially separated excitons. The maximum energy separation between the two excitons under which hybridization can occur is limited by their interaction strength with the cavity photon. Wainstain *et al.* [77] showed a hybridization of the two GaAlAs/GaAs quantum well exciton states that were separated by 4 meV, whereas Lidzey *et al.* demonstrated a hybridization with 60 meV separation in organic microcavities.

A similar case has also been reported for optical microcavity by Holmes *et al.* [36], in which a cavity photon exhibited a hybridization with the two transitions of one single material (polycrystalline organic 3,4,7,8 napthalenetetracarboxylic dianhydride (NTCDA) film) with energy separation of approximately 200 meV. The authors concluded that this was possible due to the narrow and intense spectral lines characteristric to their material. For the first time, we present a case in which the hybridization of the excitons is mediated by the SPP rather than the cavity photon, with the energy separation of the excitons being substantial 160 meV. Interestingly, our observation is very similar to one of Holmes *et al.*, even when for R6G the two transitions are very broad. Note that in both cases the two exciton states are present in one molecule, and thus we cannot talk about spatially separated excitons.

For the analysis, a coupled oscillator model was used. In the basis of the uncoupled eigenstates of SPP, R6G absorption maximum and absorption shoulder ($|SPP(k)\rangle$, $|Ex1\rangle$ and $|Ex2\rangle$), the Schrödinger's equation of the system can be written as

$$\begin{bmatrix} E_{SPP}(k) & V_1 & V_2 \\ V_1 & E_{Ex1} & 0 \\ V_2 & 0 & E_{Ex2} \end{bmatrix} \begin{bmatrix} \alpha \\ \beta \\ \gamma \end{bmatrix} = \epsilon \begin{bmatrix} \alpha \\ \beta \\ \gamma \end{bmatrix} \qquad (3.6)$$

where $E_{SPP}(k)$, E_{Ex1} and E_{Ex2} are the energies of the uncoupled SPP, R6G absorption maximum and shoulder, respectively. V_1 (V_2) is the coupling strength between SPP and R6G absorption maximum (shoulder). The strongly coupled modes can be described by a superposition of the uncoupled states with coefficients α, β and γ for SPP and R6G absorption maximum and shoulder respectively. The energies of the strongly coupled system are then obtained by diagonalization of the above Hamiltonian.

The relative weights ($|\alpha|^2$, $|\beta|^2$ and $|\gamma|^2$) of the center branch for 200 mM and 50 mM concentration samples were deduced, see Fig. 3.8. We first deduced the dispersions of the uncoupled modes by calculating a theoretical SPP curve for Ag film with 50 nm of SU-8 on top. For the two excitons, we approximate their energy by two horizontal lines whose energies are given by the two gaussians fitted to the experimentally measured absorption curves of the reference sample having no silver. Note that these energies shift slightly when the concentration is changed (see the normalized absorption spectra in Fig. 3.13). To deduce the dispersion of the strongly coupled modes, we used the above model, in which the coupling strengths of both excitons and SPP are deduced from the experimental data, that is, from the amount of splitting. As can be seen, there is a reasonable agreement between the theoretical and experimental dispersions, even without any fitting parameters.

Note that for 200 mM sample where the coupling strength is large, a substantial fraction of the hybrid mode is exciton-like: the relative coefficients for the two excitons are close to 40 percent, with only 20 percent of SPP. This clearly demostrates the hybridization of the two excitons. By comparing the relative coefficients for the two concentrations, one can see how the SPP fraction goes up and the relative exciton fractions go down as the concentration is decreased: this demonstrates how the coupling strength affects the hybridization.

3.3.5 Transition linewidth narrowing

While the large oscillator strengths are a characteristic feature of organic semiconductors, the large exciton linewidths that result from inhomogeneous broadening and the presence of a vibronic progression make strong coupling difficult to observe [52]. It is generally accepted that the split should be bigger than the individual linewidths of the uncoupled transitions [37, 35]. This is due to fact that repetitive energy transfer between SPP and R6G is not possible if one or the other loses the energy via dissipation before even one cycle is made. This is the reason why majority of the experiments are made with J-aggregates, for which the absorption linewidths are very small even at room temperature [53].

In Fig. 3.9 is shown the normalized R6G and the J-aggregate absorptions. The R6G absorption is shifted in energy to allow a better comparison. For R6G, the measured absorption is very broad (FWHM = 230 meV). Further there is a shoulder in
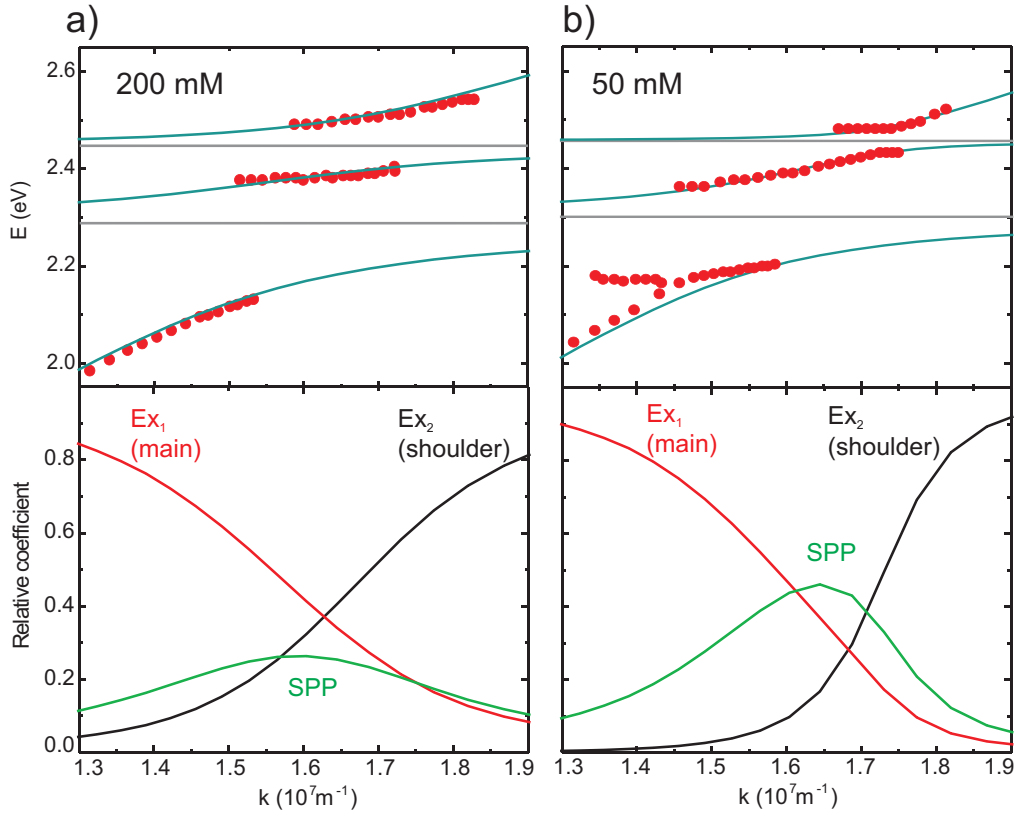
FIGURE 3.8 a) The theoretical and measured dispersions (DM2) for 200 mM sample (top) together with relative coefficients of the middle energy branch calculated from the theoretical dispersions (bottom). b) The same as in a) but for the 50 mM sample.

the absorption accompanied with a large Stokes shift (100 meV) and their role for the strong coupling studies was not initially clear.

To study the linewidths of the *strongly coupled modes*, we plotted the full width at half maximum of the three modes for 200 mM sample as a function of energy (the spectra obtained with DM2 were used, see Fig. 3.10). A clear dip in the linewidths is seen particularly in the vicinity of the low energy splitting. A similar linewidth narrowing was reported by Sugawara for J-aggregates and localized plasmons in metallic spherical nanovoids [72]. In the present case we show that linewidth narrowing is also observed in the case of propagating SPPs. However, it requires further studies to fully understand the origin of this effect.

3.3.6 The energy transfer

In this section we will demonstrate how DM1 in conjunction with DM2 can be used to study further the time evolution of the system. Since the absolute spectral intensities for these two methods are not comparable without careful calibration of the light collection efficiencies, we restrict our analysis to relative changes in the
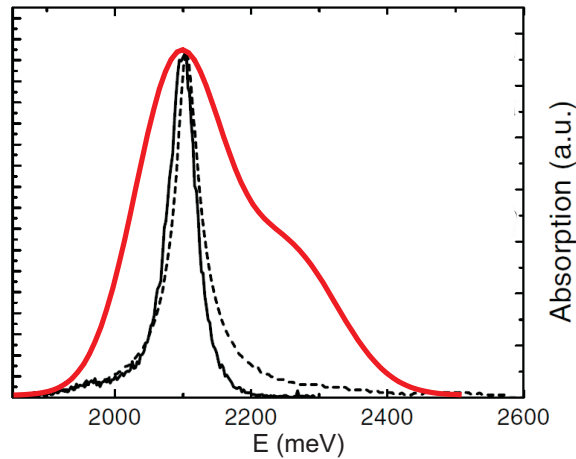
FIGURE 3.9 The measured absorption for 200 mM R6G film (red line) and the absorption (dashed black line) and the luminescence (solid black line) of the J-aggregate film used in [9]. Adapted with permission from [9].
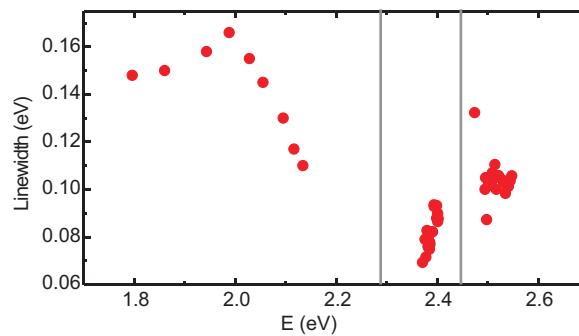
FIGURE 3.10 The linewidths of the three modes for 200 mM sample as a function of the mode energy, measured with DM2. The gray vertical lines indicate the enegy positions of the two splits.

measured spectra. To ease the comparison, the spectra measured with DM1 are subtracted from the background spectra, that is, from the white light source spectrum. Consequently, the incoupled modes are now shown as peaks rather than dips in the spectra as previously. In the Fig. 3.11 are shown the two spectra measured with DM1 and DM2 from the 200 mM sample while keeping the excitation intensity and the angle the same. The spectra are normalized with respect to highest peak, that is, the lowest energy hybrid mode peak. By comparison, two major differences can be identified. First, the spectral peak positions of the three modes are shifted in DM2 as compared to DM1. This is in accordance with previous dispersion relations in which it was shown that the split seen with DM1 is increased when using DM2. As mentioned earlier, we believe this change is due to increased interaction time of the modes measured with DM2. Second, the relative intensities of the high energy

modes are decreased for DM2. The highest and middle energy branches have only 1/4 and 1/6 of the intensities in DM2 as compared to DM1. As discussed previously, since the excitation is the same for the both methods, we expect that any difference in the results originates from the dynamics, i.e., the events taking place after the excitation. The dynamics may include several different phenomena, namely propagation speed, scattering and losses via coupling to the environment. Next we will discuss the possible mechanisms that could result in such differences in the measured spectra.
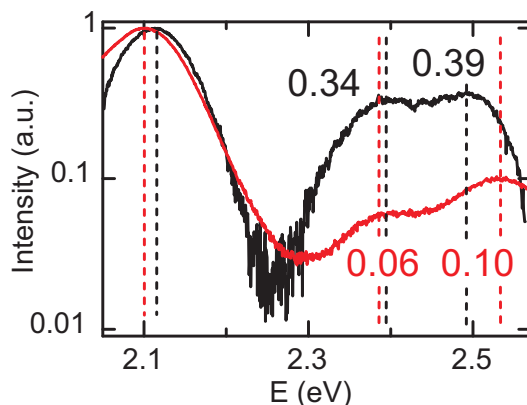

FIGURE 3.11 The normalized spectra for the 200 mM sample with DM1 (black) (background subtracted), and DM2 (red), both with excitation light angle 71.5°. The dashed lines show the spectral peak positions for the measurement methods DM1 (black) and DM2 (red). The numbers indicate the intensities of the peaks. Modified with permission from the paper **III** of this thesis.

The role of dissipation. The dissipation in the system may originate from the electron phonon interaction in the metal, in organic dye molecules (vibrational relaxation) or the surrounding SU-8 solid matrix. We note that these losses are also present when using DM 1, but with smaller effect on the system. The timescale for the losses to affect signal 1 equals the time of the incoupling event, whereas the time for the losses to affect the signal 2 extends from the incoupling event to the scattering event. The dissipation related to plasmons and to molecular vibrational relaxation are expected to be energy dependent. For plasmons, the dissipation increases monotonously with increased energy, and therefore it does not provide explanation for the observation that the middle energy branch is mostly attenuated.

The role of vibrational relaxation of R6G can be twofold: first, it could simply decrease the population of a branch by emitting a phonon. This would then be detected as decreased intensity of a given branch. Second, the dissipation may provide a pathway to decrease the population of upper energy branch while increasing the population of the lower energy branch, accompanied by the emission of a phonon that carries away the excess energy.

53

The role of mode propagation speed. Assuming the mode scattering into photons takes place in specific locations on the sample, for example in corrugations of the silver surface, the different propagation speed of each mode affects the total time the mode spends in the system before scattering. The slower the mode, the longer the time and higher the dissipation prior to scattering. Provided that the mode propagation speed is equal to the slope in the dispersion curves, the middle energy branch has the smallest propagation speed of the three branches, and would thus be the subject to highest dissipation.

The role of the mode scattering cross section. The scattering cross section of the coupled modes may be energy (wavelength) dependent and this could account for the difference between the obtained spectra. Our previous work indicates that no significant wavelength dependency for plasmon scattering can be seen within 450-550 nm. Also, a strong wavelength dependence of scattering should affect the measured spectra for DM2, thus altering the dispersions measured by this method. Thus, the very high resemblance of the dispersions measured with DM1 and DM2 for the sample having only silver (see Fig. 3.2) renders this option unprobable.

The role of energy transfer between the modes Finally, we want to discuss the possibility of the population transfer between the strongly coupled branches. The energy transfer between strongly coupled modes has been predicted [1] and experimentally addressed for inorganic [77] and organic [50] microcavities containing J-aggregates and the qualitative agreement between the experiments and a model assuming energy transfer was found. Agranovich *et al.* [2] suggest that the majority of exciton states in J-aggregate microcavities are in fact incoherent. These states occupy the very high and low k vector states at the resonance energy, forming a reservoir of excitons that can be pumped nonresonantly, and which by decay populate the coherent low energy hybrid modes.

Unpublished data by the author of this thesis implies this could be the case in our system as well. A continuous, but nonresonant SPP excitation of the high energy branches in Kretschmann configuration yields to the population of the lowest energy branch, but no significant population is seen in the upper branches except at the energy of the excitation light. This suggests that 1) the population from the high energy branches is indeed transferred to the lowest energy branch, and that 2) the principal relaxation pathway of the high energy branch modes to the lowest branch is connected to the vibrational relaxation of R6G. Whether the relaxation results to a direct population transfer to the lower energy branch, or to population transfer first to the uncoupled exciton reservoir at high k vector states and then to the lower energy branch, remains a question. However, as evidenced by the leakage radiation experiments of such a system, the low energy population is still strongly coupled and exhibits a band bending (anticrossing) at the energy of the R6G absorption maximum.

3.3.7   The conversion of the hybrid modes to photons

In previous SPP-molecule strong coupling experiments only the lowest energy branch can be made to emit light [74,75,9]. This is in conrast to microcavity experiments, in which also the high energy branches are luminescent. However, a reduced intensity of the high energy branch luminescence has been observed also in microcavities, and has been explained by the fast population transfer between the branches, occurring on time scales of 30 fs, which is much faster than the normal radiative decay of polaritons [54].

Here we show that also the high energy SPP-exciton hybrid modes can be converted to photons. In Fig. 3.11 is shown the luminescence spectrum measured from the 50 mM sample with DM2, exhibiting emission from all three strongly coupled modes. Further, in waveguide samples (see Fig. 3.7) the emission of the high energy branches is seen as well, with very sharp spectral features. Since the conversion of the modes to photons is important in terms of both applications and fundamental physics, it would be of interest to evaluate what are the particular conditions for light generation of the high energy modes.

In our studies regarging thin film samples, the excitation has been done with white light in Kretschmann configuration when detecting the luminescent light from the molecule side of the sample. This is in contrast to other studies with similar samples where the system has been excited nonresonantly with laser light from the molecule side of the sample, while observing the leakage radiation with a reverse Kretschmann geometry [74,75,9]. Also the luminescence from the molecule side has been measured in such a configuration, exhibiting only the uncoupled emission of the molecules [74,75,9]. In this case it is possible that while using a laser to directly excite the molecules also the dipole orientations that are not strongly coupled to SPPs are excited and their contribution to luminescence screens out the strongly coupled mode luminescence.

3.3.8   Monomers or aggregates?

Next we will estimate the relative fractions of R6G dimers and monomers in our samples and their contribution to the observed results are discussed. It is well known that R6G molecules have a tendency to form aggregates, especially dimers in high concentrations. In Ref. [10], Bojarski studied the absorption of R6G in solid polyvinyl alcohol polymer matrices, and was able to extract both the monomer R6G as well as J and H dimer contributions of the absorption. Our estimations are based on the measured absorbances of the reference thin film samples having no silver together with the analysis carried out in Ref [10]. In Fig. 3.12 is shown the monomer and dimer absorbances measured in [10], together with the 25 mM reference sample used in our experiments. The high resemblance between the spectrum of our sample and the monomer spectrum implies that the 25 mM sample consists of monomers only.
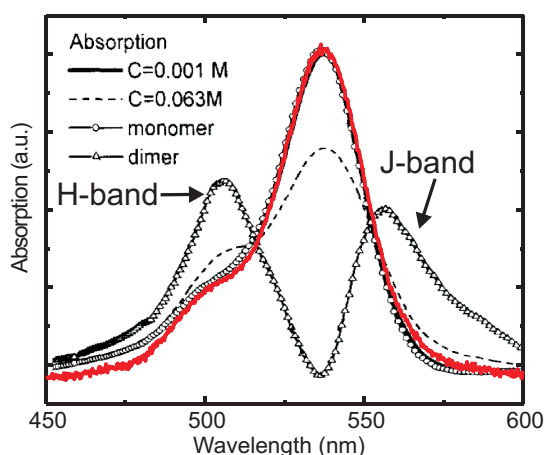
FIGURE 3.12 The measured absorbances from the 25 mM sample (red curve) together with the results from [10] Modified with permission from [10].

Since the dimer concentration should scale with the total R6G concentration, the 4 mM sample likely consists of only monomers as well. (The 25 mM sample was used for comparison due to low signal-to-noise ratio in 4 mM sample). To analyze the two higher concentration samples, we note that while the dimer H band and the monomer shoulder absorptions overlap, there is no dimer absorbance at monomer absorption maximum. Thus the relative height of the absorption shoulder should go up when the dimer concentration is increased. In Fig. 3.13 is shown the normalized absorbances of the reference samples, showing that when the R6G concentration is increased, the shoulder absorption is increased, as expected. The relative increase of the shoulder absorbance accounts for the increased amount of aggregates. Note also the slight red shift or broadening of the main absorption; this is likely due to J-dimer contribution. The H-aggregate fraction of the R6G in our samples could be deduced by 1) fitting a Gaussian curve to the shoulder and the maximum absorption, 2) comparing the integrated area of the shoulder to the shoulder area of the monomer absorption. From this, we estimated the contribution of H dimers to the total absorbance at the shoulder energy to be 0, 0, 15 and 65 percent for the 4, 25, 50 and 200 mM samples, respectively.

As the low energy split in our thin film samples is located at the monomer absorption maximum rather than the dimer J band maximum, we conclude that this split originates from the R6G monomers. The high energy split is visible with relative small H-aggregate concentrations (15 percent), and therefore we expect that both the monomers and dimers may contribute to that splitting.
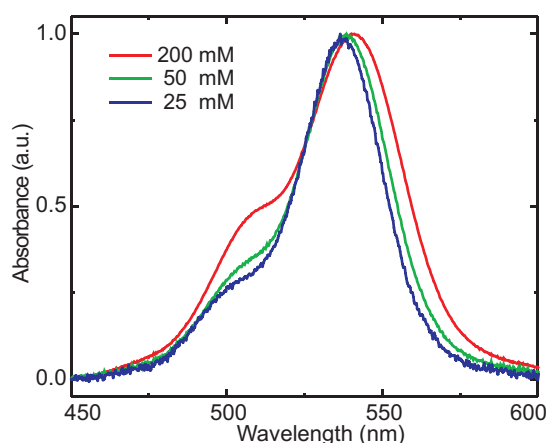
56

FIGURE 3.13 The normalized absorbances from the 25 mM, 50 mM and 200 mM reference samples.

3.4 Discussion

Based mainly on the paper **III** of this thesis, in this chapter we have presented a series of new findings related to room temperature coherent interaction between the SPPs and organic molecules. In particular, we report on

1) Observation of strong coupling and vacuum Rabi splitting in broad absorption molecule (R6G), implying that the strong coupling may readily accessible at room temperature for a variety of other SPP-molecule systems as well. This should be taken into account in future studies and applications.

2) Observation of *double* splitting, in which SPP mediates the hybridization of the two molecular excitations.

3) Transition linewidth narrowing for propagating SPP-molecule system in the vicinity of the strong coupling condition.

4) A novel detection method (DM2), which gives access to probe the time evolution, such as energy transfer and relaxation dynamics of the system when used in conjunction with DM1.

5) A lithographic method to control the interaction time of the SPP-molecule system, allowing to transit from weak to strong coupling regime with high precision. The interaction time is a key parameter in understanding and controlling the strong coupling dynamics. The method allows a sub-fs control over this parameter by means of standard electron beam lithography. The summary of the effects of the interaction time on the strong coupling are presented in Fig. 3.14.

6) The possibility of further increasing the SPP-molecule coupling by introducing a *cavity-SPP*, in which the decay to free-space photons is prohibited. The method for fabrication of such a cavity is straightforward and can be done by standard lithography methods.
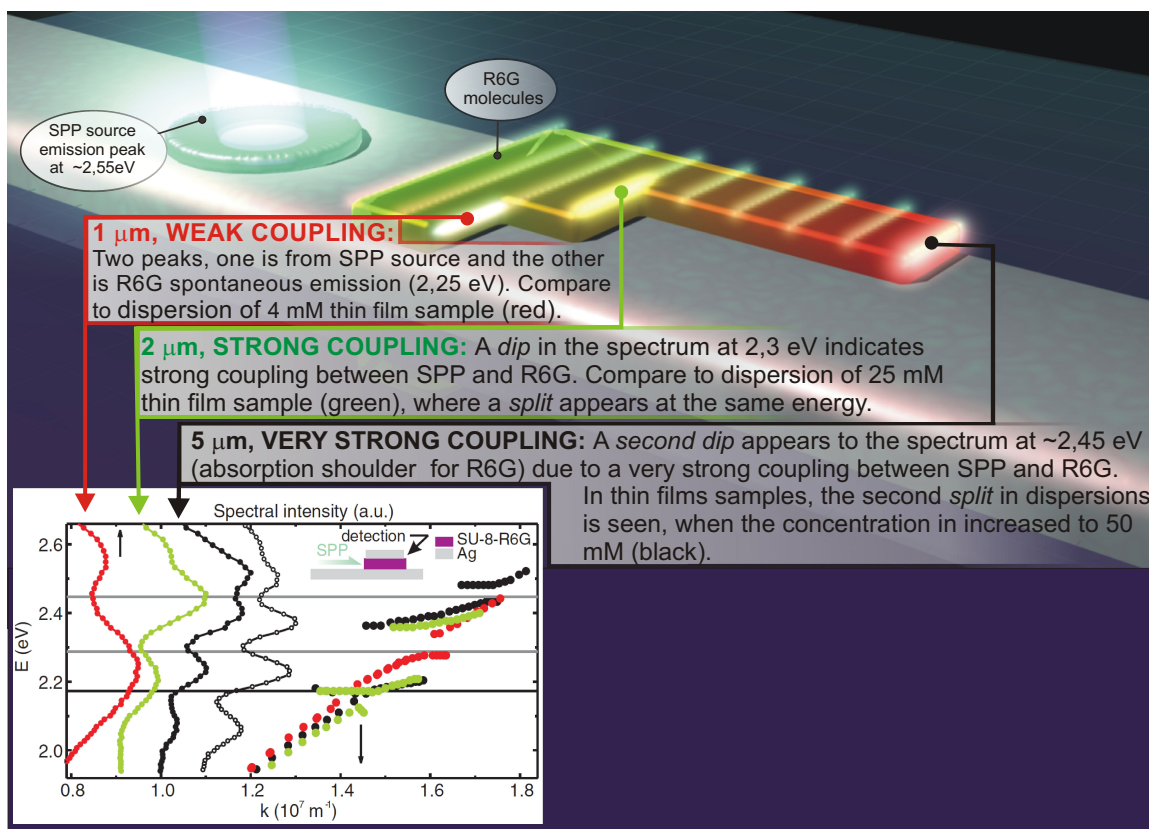
1 μm, WEAK COUPLING: Two peaks, one is from SPP source and the other is R6G spontaneous emission (2,25 eV). Compare to dispersion of 4 mM thin film sample (red).

2 μm, STRONG COUPLING: A *dip* in the spectrum at 2,3 eV indicates strong coupling between SPP and R6G. Compare to dispersion of 25 mM thin film sample (green), where a *split* appears at the same energy.

5 μm, VERY STRONG COUPLING: A *second dip* appears to the spectrum at ~2,45 eV (absorption shoulder for R6G) due to a very strong coupling between SPP and R6G. In thin films samples, the second *split* in dispersions is seen, when the concentration in increased to 50 mM (black).

FIGURE 3.14 The summary of the effects of the interaction time on the strong coupling. The emission spectra measured from the waveguide samples having different lengths of R6G deposited on top of a waveguide, along with the dispersion curves of the thin film samples with different R6G concentrations. The red, green and black spectra correspond to 1 μm, 2 μm and 5 μm lengths of R6G, respectively. The black spectrum is measured from a waveguide sample having a 5 μm R6G area as well, but with a layer of silver deposited on top this area (see the schematic inset). In the dispersions red, green and black correspond to 4, 25 and 50 mM samples, respectively. Modified with permission from the paper **III** of this thesis.

Taking into account the complexity of the overall system, the coherent interaction of the molecular ensemble with the SPP in room temperature is remarkable: a SPP-quantum consists of a macroscopic number of conduction band electrons in the vicinity of the metal surface, which in practical systems is far from flat. Further, even only one organic dye molecule has innumerable amounts of electonic transitions, couplings to environment via vibrations, etc. Taking into account the disorder that is present in such an organic film with an ensemble of molecules (different dipole orientations of the molecule, aggregates of the molecules, variations in the thickness of the layer and impurities), it is not intuitively clear why such a system should exhibit any coherence whatsoever. However, SPP systems have been shown to exhibit coherence in many room temperature studies, including preservation of entangle-

58

ment in photon-SPP-photon conversion [26], SPP mediated emission of antibunched photons from single emitter [3], and double slit experiment [83].

Chapter 4

Field induced nanolithography for high throughput pattern transfer

Roughly, the fabrication of nanostructures can be divided to top-down and bottom-up methods. Together these two complementary methods create a powerful basis for novel designs with increasing complexity and function. As the traditional top-down fabrication methods were inherited from the IC-industry to the study of nanosciences, soon after a set of bottom-up methods were invented that relied on the properties of the materials themselves to form the desired configuration. Examples of nano-objects created by such methods include quantum dots (QDs), carbon nanotubes, DNA origamis [68] and various polymers. Often these objects are extremely well defined in terms of their chemical composition. For example, in DNA origami the position of each individual base-pair can be controlled, in carbon nanotubes the chirality defines whether the tube is metallic or semiconducting, and in QDs their light emission properties can be tailored by the choice of material and the size.

However, practical devices often require several elements with different properties coupled to each other to achieve the desired function. For example, a carbon nanotube needs to be connected to a set of electrodes to make a transistor. The coupling between these elements is fundamentally bound to their relative position. As the precise spatial control over each of the device components has proven to be exceedingly difficult, nanocircuits and devices with high complexity, packing densities and structural order over large sample areas have not yet been realized.

Due to both scientific and commercial interest to control the spatial position of individual nanoparticles, several methods have been introduced, utilizing fluidics [69], magnetic fields [69] and electric fields. For electric fields, particularly electrophoresis [20], light-induced electrophoresis [33], dielectrophoresis [46], light-induced dielectrophoresis [15], optical tweezers [43], and surface plasmon polaritons have been used [66].

Many of the presented methods enable precise control of individual particles [43, 20, 67, 22]. However, they are limited in throughput which rules out their

use for mass production. On the other hand, the methods enabling high throughput are often restricted in spatial resolution [16, 33]. A second limitation is that the particles are bound to the master chip [76, 66, 69, 46] and thus do not allow repetitive pattern transfer which is crucial for mass production. A recently introduced high throughput pattern transfer method utilizing electrophoresis in conjunction with polymerizable target surface addressed many of the above issues, but the method is applicable to charged particles only [14].

NanoImprint Lithography (NIL) has proved to be a valuable tool for high throughput, high resolution transferring. NIL uses a topologically patterned mold to transfer the pattern onto a target surface. Usually the surface is covered with a thin layer of resist [18], although approaches with no resist have also been developed [17, 38]. Microcontact printing (μCP) uses a similar mold as NIL, but made of flexible polymer Polydimethylsiloxane (PDMS) that can be used to directly deposit self-assembled monolayers of molecules or other nano-objects to the target surface. μCP has been successfully used particularly in bioapplications. A variant of this method was recently introduced, which allowed a high throughput deposition of colloidal (60 nm) gold particles with high reproducibility and single particle resolution onto the target plate [45].

While NIL and μCP can be used to produce high throughput pattern transfer, the mold (master) for each pattern is unique. For such a method to be applicable in the fabrication of *multicomponent* nanodevices, the precision of the two (or more) overlay patterns should be around 10 nm or less. The challenge here is to align the second mold with such a precision with respect to already existing pattern. Surely, this could be done using a piezo actuated interferometric position system as in state-of-the-art electron-beam writers, but this approach is far from straightforward. Thus it is highly desirable to introduce a *universal* stamp capable of producing arbitrary pattern onto target without changing the master. In this case, the only relative movement required between the target and the master could be established by one single piezo stage moving in a direction normal to the master and target surfaces. The second layer could then be produced just by changing the pattern of the master and then contacting the master again with the target by using a piezo. In such a configuration, the relative alignment of the master and the target remains the same between the consecutive layer depositions, and thus the overlay alignment is always correct even in the absence of a positioning system.

We propose a high precision, high-throughput method for pattern transfer of nanoscale objects. The feasibility of this dielectrophoresis (DEP) based method is demonstrated by producing arrays of quantum dots. The method can be extended to arranging carbon nanotubes, biomolecules and other nano- and microscale objects into desired configurations. In our method, the pattern on a master stamp can be dynamically controlled by electromagnetic fields and transferred to another surface, while the master stamp stays intact. The dynamic control over the trapping pattern

can be used to realize one single, universal master stamp capable of transferring any desired multicomponent pattern to the target surface. Due to parallel nature of both the trapping and the pattern transfer, this method holds a potential for mass fabriction of nanostructures.

4.1 Dielectrophoretic force

A particle and its surrounding medium in the electric field $\vec{E}$ can be considered as an effective dipole which has an induced dipole moment $\vec{p}$, that is proportional to the electric field [39, 44], i.e.,

$$\vec{p} = \alpha \vec{E}. \tag{4.1}$$

The constant $\alpha = \alpha(\omega, r_\mathrm{p})$ is the effective polarizability of the object, which depends on the angular frequency of the electric field ω, the radius of the particle r_p and the properties of both the particle itself and the surrounding medium. Note that this enables the tailoring of the polarizability by the proper choice of medium. Polarizability of a particle of volume V with a permittivity ϵ_p is

$$\alpha = 3V\epsilon_p Re[K]. \tag{4.2}$$

Here Re denotes the real part, and K is so-called Clausius-Mossotti factor, which depends on both the particle and the medium, and is described by Zheng et al. [82]

$$K = \frac{1}{3}\frac{\epsilon_p^\star - \epsilon_m^\star}{\epsilon_m^\star + A(\epsilon_p^\star - \epsilon_m^\star)}, \tag{4.3}$$

where, A is a geometrical factor ($A = \frac{1}{3}$ for a sphere).

The complex permittivities of the particle and medium, $\epsilon_p^\star$ and $\epsilon_m^\star$ respectively, are given by

$$\epsilon_p^\star = \epsilon_p - i\frac{\sigma_p}{\omega} \tag{4.4}$$

and

$$\epsilon_m^\star = \epsilon_m - i\frac{\sigma_m}{\omega}. \tag{4.5}$$

In these equations, ϵ_p and ϵ_m are the real parts of the permittivities, and σ_p and σ_m are the conductivities of the particle and the medium, respectively.

The dielectrophoretic force $\vec{F}_\mathrm{DEP}$ exerted to the particle by the nonuniform electric field is given by

$$\vec{F}_\mathrm{DEP} = (\vec{p}\cdot\vec{\nabla})\vec{E} = \frac{\alpha}{2}\vec{\nabla}(E^2). \tag{4.6}$$

For an isotropic homogeneous spherical particle with radius r_p, the time-averaged

dielectrophoretic force is

$$\vec{F}_{\mathrm{DEP,tav}} = 2\pi\epsilon_m r_{\mathrm{p}}^3 Re \left[\frac{\epsilon_p^\star - \epsilon_m^\star}{\epsilon_p^\star + 2\epsilon_m^\star} \right] \vec{\nabla}(E_{\mathrm{RMS}}^2),$$ (4.7)

where E_{RMS} is a root-mean-square value of the electric field (assuming a sinusoidal time dependence).

As seen from the Eq. 4.3 Clausius-Mossotti factor K is a frequency dependent variable, with real part varying from -0.5 to +1. When $Re[K] > 0$ ($Re[K] < 0$), the force exerted on the particle is directed towards the field maximum (minimum). These two regimes are termed as positive and negative dielectrophoresis, respectively.

An example of a frequency dependence of the Clausius-Mossotti factor is shown in Fig. 4.1.
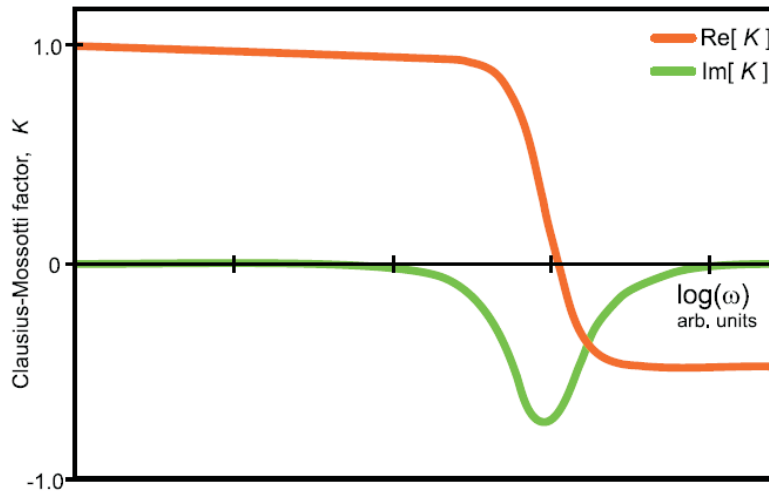

FIGURE 4.1 Frequency dependence of Clausius-Mossotti factor for a spherical particle.

Several notifications about the Eq. 4.7 should be made.

- By changing the frequency of the electric field, the Clausius-Mossotti factor can change from positive to negative, which causes the DEP force on the particle to change its direction accordingly. This unique property of Clausius-Mossotti factor of the particle under a specified suspending medium can be utilized to manipulation of particles.

- The DEP force is proportional to the size of the particle, which poses a challenge for the manipulation of nanoscale particles. However, the equation is derived using classical description of permittivity and conductivity, which are derived as bulk values, and may thus not be exactly valid in the case of

nanoparticles or macromolecules, where a significant fraction of the atoms of the object reside on the surfaces.

- The direction of the DEP force does not depend on the direction of the electric field, since the field gradient causes the force on the particle, not the field itself. In the case of ac field, the particle experiences time-varying force, but the direction of the force is always the same, even though the direction the electric field vector is changing in time. Thus, it is sufficient to consider only a time-averaged values as done in Eq. 4.7. Consequently, even the equation represents the DEP force in the case of an ac electric field, it is valid also for a dc electric field.

To be able to trap particles using DEP, the DEP force must overcome the Brownian motion, which can be treated as a random force, i.e., so-called drag force, whose maximum value is given roughly by [63]

$$F_{thermal} = \frac{k_B T}{2 r_{\mathrm{p}}},$$ (4.8)

where k_B is the Boltzmann constant, T is the temperature, and r_{p} is the radius of the spherical particle. This sets the minimum particle size that can be manipulated using certain DEP force. Since the thermal drag force ingreases with decreasing particle size, a higher DEP force is needed in order to manipulate nanoscale particles. The higher field gradients, which are needed to create a higher DEP force, can be generated by reducing the electrode dimensions or increasing the voltages applied to the electrodes. However, due to practical reasons, e.g., use of aquatic solution or rigidity of the electrode structure, the applied voltage cannot be increased too much. Also, the Joule heating in the solvent can cause fluid currents that limit the trapping.

4.2   The proposed method

The proposed method, Field Induced Nanolithography (FINAL), relies on the forces exerted to the polarizable nano-objects in non-uniform electric fields. These fields can be conveniently realized and dynamically controlled by applying suitable voltages to nanoscale electrodes structured on a master stamp surface. To estimate the trapping force of the system, we used 3 dimensional finite element method modelling to deduce the gradient of the electric field square in the vicinity of the nanoscale electrodes, see Fig. 4.2a. The electrode geometry used in the experiments was imaged with AFM and then implemented into the simulation model (see Fig. 4.2b). A dc voltage of 2.47 V was applied to the elecrodes, which corresponds to the RMS value of the actual sinusoidal voltage used in the experiments. Previously it was shown that if the RMS value of the voltage is used in the calculation the time-

averaged force acting on a particle is $F_{DEP,tav} = \alpha \left|\nabla E^2_{RMS}\right|$, where α is the polarizability of the particle. With $\alpha/\epsilon_0 = 2.8 \times 10^7$ Å^3 for the used quantum dots [43], one can estimate the force to be 1.3×10^{-10} N, which is well above the brownian force 4×10^{-13} N acting on a 10 nm diameter particle at room temperature. It is exactly the extremely high field gradients produced by such electrode structure that makes the overall pattern transfer procedure very robust.

Further, the simulation shows that the field gradients produced by the small electrodes are tightly confined to the gap region, allowing a trapping to predefined locations, having a spatial resolution that is basically defined by the resolution of the electrode fabrication process.
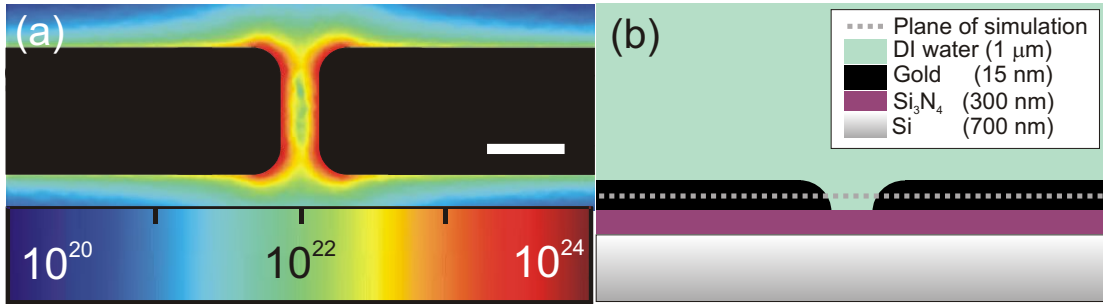

FIGURE 4.2 a) Finite element method simulation of $\left|\nabla E^2\right|$ (in units V^{2}m^{-3}) for the electrode geometry used in the experiments, 5 nm above the surface of the Si/Si$_3$N$_4$ substrate (Modified from the paper **IV** of this thesis). The scale bar is 100 nm. b) The sideview of the simulated structure.

In Fig. 4.3a-d is shown a schematic of the overall transfer procedure. Since the master stamp is reusable, this procedure could be repeated several times, for a variety of different nano-objects if desired. For each cycle, the trapped pattern can be controlled by only changing the voltages applied to the electrodes. Thus, a one single versatile master stamp having a two dimensional eletrode array could be used for transferring any multicomponent pattern to the surface. The preferential adhesion to the target plate can be realized by modifying the surface of the master stamp with adhesion-blocking chemicals, and the target surface with adhesion-enhancing chemicals.

4.3 Experimental

The fabricated electrodes consisted of a 2 nm thick layer of Ti and 15 nm of Au and they were fabricated on a Si/Si$_3$N$_4$ substrate using standard electron beam lithography. The metals were deposited in ultra high vacuum with electron beam evaporator. The structure used in this experiment consisted of a row of 170 nm wide fingertip electrodes with 50 nm gap (see Fig. 4.2). Watersoluble CdSe (core) / ZnS (shell) /
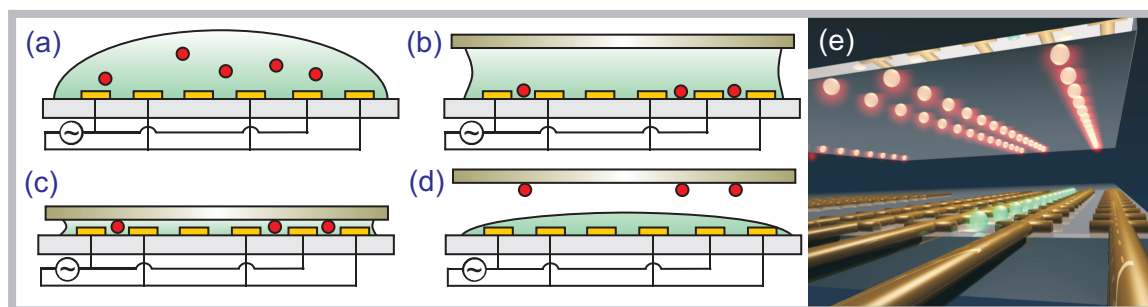
FIGURE 4.3 The field induced nanolithography (FINAL) method: the principle. (a) The ac voltage is applied to a certain set of electrodes on a master stamp to produce the desired field pattern, and the solution containing nano-objects is injected. (b) The dielectrophoretic forces trap the nano-objects to the location of strongest electric field, which is followed by bringing a target plate in contact with the solution. (c) The target plate is brought in mechanical contact with the trapped nano-objects. (d) The target plate is lifted with the nano-objects attached. (e) An artistic view of the trapping of the second species of objects after the first pattern transfer. Modified from the paper **IV** of this thesis.

polyethylene glycol (coating) QDs having an emission wavelength of 655 nm used in this work were purchased from Invitrogen. The preferential adhesion to the target surface rather than to the master stamp was realized by incubating the master stamp with a solution preventing nonspecific binding (SuperBlock blocking buffer in PBS, from Pierce), and the target surface with Poly(Diallyldimethylammonium chloride) (PDACMAC) solution which enhances adhesion.

The applicability of the proposed method was verified by first producing arrays of quantum dots onto predefined configurations and subsequently transferring this pattern to a target plate. The specific steps of the procedure were as follows. **Step 1**: A sinusoidal voltage signal (amplitude 3.5 V, frequency 1 MHz) was applied between the opposing electrodes (Figs. 4.3 and 4.4a) and kept on throughout the rest of the experiment. A 80 nM quantum dot solution was injected onto a master stamp, which was followed by a 10 min wait time for the trapping to take place. **Step 2** (optional): To decrease the concentration of free, non-trapped quantum dots in the solution, we injected additional de-ionized water onto a master stamp, and then removed it. This step was repeated several times. Also a reference sample was made for which this step was omitted. **Step 3**: The target plate (glass treated with PDAC-MAC) was manually brought in contact with the solution (Figs. 4.3b and 4.4a). **Step 4**: The target plate was further lowered to contact the master stamp and the trapped quantum dots (Fig. 4.3c). **Step 5**: The target plate was removed and dried with nitrogen flow (Figs. 4.3d and 4.4c) and the master stamp was rinsed with DI water and dried.

The dielectrophoretic trapping of quantum dots was verified by in-situ monitoring with confocal microscope during the trapping procedure, see Fig. 4.4a. The
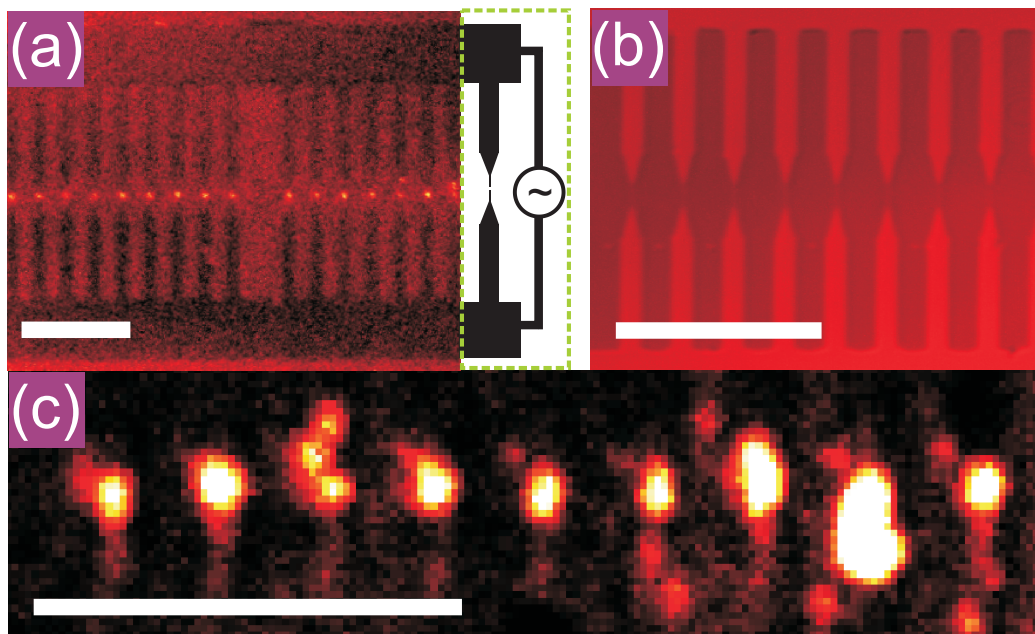
FIGURE 4.4 The field induced nanolithography (FINAL) method: a demonstration. a) A confocal fluorescence image of the master stamp having a fingertip electrode structure (see Fig. 4.2). The imaging is made through the target plate during the dielectrophoresis. The dashed part shows the schematic of the electrodes and the circuit wiring. (b) The image of the master stamp after the transfer process (see Fig. 4.3d). (c) The image of the target plate after the transfer process (see Fig. 4.3d) demonstrates the efficient transfer of the pattern. The scale bars are 50 μm. Adopted from the paper **IV** of this thesis.

imaging was made through a standard microscope cover slip which was also used as a target plate for the pattern transfer. As can be seen, the trapping takes place within the electrode gap with high reproducibility. After the transfer procedure, the master stamp appears to be virtually intact and free of quantum dots (see Fig. 4.4b), which enables the re-use of the stamp. Figure 4.4c shows the confocal microscope fluorescence image of the target plate after the transfer procedure. The spacing between the high intensity spots coincides exactly with the inter-electrode spacing of the master stamp, which confirms that the transferred pattern is indeed originating from the dielectrophoretically trapped quantum dots of the master stamp. To verify that the overall procedure induced no changes to the optical properties of the QDs, their emission spectra were measured before and after the transfer to the target plate, with no detectable changes. Note that while the signal in the trapping location is so high that the confocal signal is saturated, the background intensity is very small. This demonstrates the selectivity of the method. Further, by introducing the step 2 the intensity ratios of the trapping location and the background could be increased 5-50 fold as compared to the sample with step 2 omitted. This implies the background intensity comes from the free, untrapped quantum dots within the

liquid that bind to the target plate when it is contacted with solution. Thus, by introducing more careful rinsing (step 2) during the trapping, one could further decrease the background. Importantly, this also implies that the already trapped quantum dots stay within the trap even during the rinsing; Otherwise there would be no significant increase in the intensity ratio.

The dynamic control of the trap and the QDs was studied by monitoring the time evolution of the system after the trap has been switched off, see Fig. 4.5. The imaging was carried out through the target plate by using a confocal microscope (see Figure 4.4a). After the ac-voltage (2.75 V amplitude, 1 MHz) has been switched off the restoring force of the trap disappears and the QDs escape from the trap due to Brownian motion, demonstrating the dynamic control of the trap. The escaped QDs are likely to be aggregates, as evidenced by their high luminescence. However, during the trapping procedure, the luminescence intensity within the trap builds up in a smooth and continuous rather than stepwise manner, implying the majority of the initially trapped objects are either individual QDs or smaller aggregates than the ones escaping the trap. Some of the QDs stay attached to the surface of the master stamp even after the trap has been switched off. This is due to nonspecific binding of the QDs. However, as can be seen in Fig. 4.4b, the master stamp is free from QDs after rinsing and drying, enabling the reuse of the stamp.
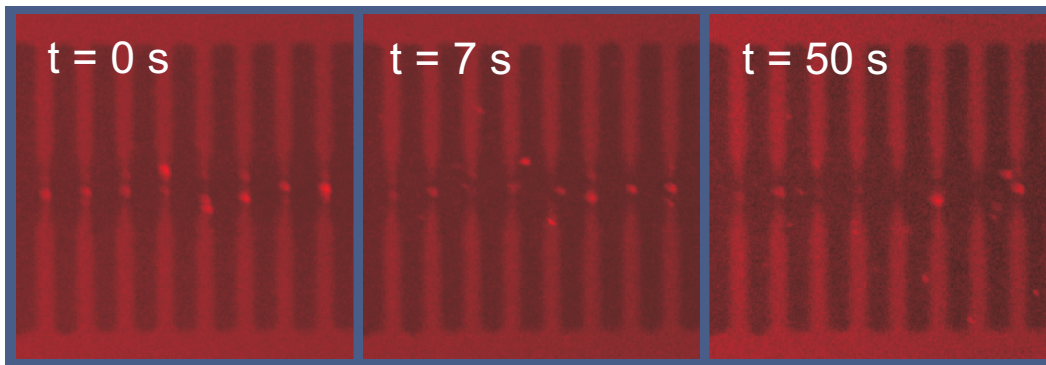

FIGURE 4.5 The time evolution of the system after the trap has been switched off at t = 3.5 s.

At present we cannot conclude whether the trapped QDs are individual ones or aggregates due to lack of sensitivity of the confocal measurement setup. In principle this could be done by monitoring a fluorescence of the trap region, where the presence or the absence of blinking would imply individual QD or plurality of QDs, respectively. However, by using the simulation results shown in Fig. 4.2a together with the polarizability of the QDs in water [43], one can make a simple estimate of the trapping force exerted to individual QDs in our system, yielding a force almost three orders of magnitude higher than that due to the Brownian motion for 10 nm particle. Thus, we expect that also individual QDs are trapped. Further, since the

electrode dimensions down to sub-10 nm scale are accessible with standard electron beam lithography methods, we expect that the technique presented here could be used to trap only one individual QD per gap as well. We also believe that it is the wealth of the trapping force of such nanoscale electrodes that enables the pattern transfer with very basic methods as reported here, i.e., by pressing the target plate manually in contact with the master.

4.4 Discussion

The advantage of using nonuniform electric fields:
Due to polarizability of a wide range of materials, the method presented here can be extended to a variety of nanoscale objects, such as individual DNA molecules, origamis, carbon and other nanotubes as well as for other, metallic insulating or semiconducting colloidal nanoparticles. In fact, as Eq. 4.8 implies, the trapping force is governed by the *effective* polarizability. Thus, objects composed of any material can be trapped with such a method, provided that the medium is chosen in a way that there is a difference between the dieletric permittivities of the two. This is advantageous as compared for example to electrophoresis or magnetic trapping which rely on the net charge or magnetic properties of the object, thus limiting the applicability of those methods to certain particular materials.

The advantage of using nanoscale dielectrophoresis:
As mentioned previously, the highly nonuniform electric field is the key requirement for successful manipulation of nanoscale particles. In nanoscale, this requirement plays even more pronounced role, since the trapping force goes down and the brownian force goes up with decreasing particle size. It can be shown that the electric field gradients created by the nanoscale electrodes produce particularly strong field gradients, which allows the manipulation of very small particles. In fact, the gradient of the electric field square is three and six orders of magnitude higher as compared to the optical tweezers and SPP based devices reported elsewhere [43,66], facilitating the control over very small objects.

In addition, the dynamic control over the trapping pattern through applied voltages allows a very straightforward method for controlling individual trapping centers in fast timescales that could be challenging to realize for example by SPP based methods, in which the electric field landscape is static and predefined by the geometry of the master. This dynamic control also allows one to create one universal master stamp that could be used to transfer complex multicomponent structure onto the target surface with high spatial precision between the overlay patterns. In addition, the parallel nature of this trapping and the pattern transfer provide interesting perspectives for mass fabrication of nanoscale circuits.

Further, we expect the power input to the system to be negligible as compared to optical tweezers or SPP based devices. This is important since the inreasing tem-

perature 1) interferes with the trapping via increased brownian force and fluid convection and 2) can destroy or deform the objects of interest that are sensitive to temperature, for example biomolecules such as DNA.

The advantages of dielectrophoresis have previously been recognized in pattern transfer by other groups as well [73,48]. Here we show that scaling the electrode geometry down to nanoscale and by combining this with pattern transfer, a 10 fold improvement in particle size and 5 fold improvement in overall feature size can be achieved as compared to previous dielectrophoresis based methods [73,48].

Challenges:

Of course it still remains a challenge to prepare a suspension out of any arbitrary material while avoiding aggregation and keeping the conductivity of the medium low enough to avoid excess Joule heating. Further, it is an open question whether the preferential adhesion to the target plate is always realizable and whether the mechanical contact would destroy some more fragile objects than QDs. One possibility would be to introduce a thin layer of polydimethylsiloxane (PDMS), a flexible polymer shown to be highly biocompatible, onto the surface of the master to establish a good mechanical contact between master and the target even with very low pressing force. Additionally, due to its very hydrophobic surface, a nonspecific binding to PDMS has been shown to be very weak, which in turn facilitates the pattern transfer to the target [45].

Future Prospects:

In addition to high throughput pattern transfer, we note that the master stamp by itself could also be used to monitor the interplay between two different nanoscale objects as a function of their relative concentration within the trap. This could be realized, e.g., by first loading one species of nano-objects within the trap, then applying step 2 to remove the excess, nontrapped objects from the liquid and then introducing a second species of nano-objects by a fluid-injection. This sort of device could be used to create nanoscopic reaction vessels within the liquid, in which the walls of the vessel would be defined by the electric field landscape rather than some physical constraints as in traditional experiments (the walls of a test tube, etc). The advantage of this approach over the traditional one would not be limited to only reduced size of the vessel, but also the dynamic control of the vessel size, shape, number and potential well depth that isolates the vessel from surroundings, would provide new perspectives to the experiments. Also, the electrodes on the master stamp offer a convenient way to study current transport, charging effects or optical properties of the QDs in the presence of nonuniform or timevarying electric fields.

Chapter 5

Ultra-high vacuum compatible electrical feedthroughs for portable Bose-Einstein condensate

5.1   Background

Bose-Einstein condensates of ultracold atoms have been experimentally realizable for several years. The realization of a condensate can be greatly simplified using a microscopic magnetic trap on a chip in a glass cell [30]. In this case, the electrical feedthroughs for current carrying wires were made by wires soldered to the connector inside the glass cell. Also, a portable configuration in which the atom chip itself forms one wall of the vacuum system was introduced [23]. A 50 μm thick mirrored silicon plate was anodically bonded to the glass cell as shown in Fig. 5.1. In this case the extra silicon plate increased the distance between the current carrying wires and the magneto-optical trap (MOT) which leads to reduced the magnetic field gradients. This in turn makes it more difficult to realize Bose-Einstein condensate in such a configuration. The thickness of the silicon plate cannot be decreased because of the mechanical strain resulting from the ultra-high vacuum inside the glass cell. Further, high currents needed to realize the BEC in such a configuration increase the temperature within the vicinity of the wires and often result to the fracture of the glue used between the silicon plate and the chip.

5.2   The fabrication of ultrahigh vacuum compatible electrical feedthroughs for BEC

In this section a novel fabrication process for feedthrough atom trapping chips, which are used in atomic condensate optics, is introduced.
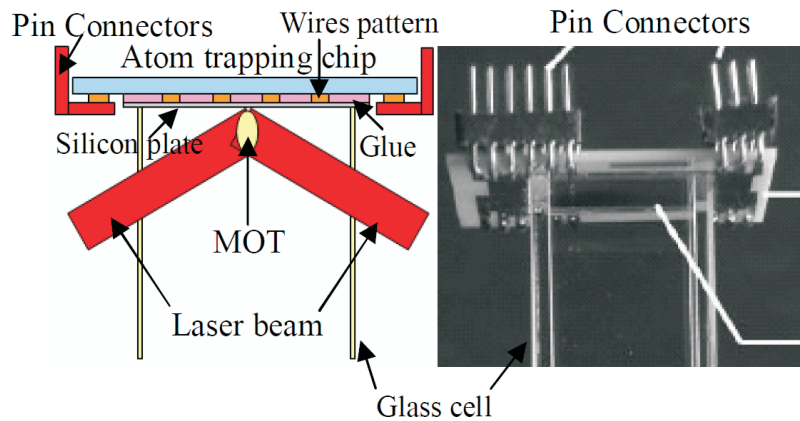
FIGURE 5.1 Schematic drawing and photograph of the portable vacuum system for Bose-Einstein condensate. Adopted from the paper **V** of this thesis.

The advantages of using feedthrough atom trapping chips are the simple microfabrication process which has a potential for mass fabrication and reduction of the overall chip area bonded to the glass atom trapping cell. Our results demonstrate that current can be conducted through the feedthoughs while still maintaining the ultra high vacuum of 1×10^{-9} torr. Our approach utilizes copper electroplating to vacuum seal the chip-through electrical feedthroughs. In electroplating, the deposition of metal is realized by using a solution containing a metal salt. By applying a suitable voltage between the object and the solution, the positively charged metal ions in the solution are attracted to the object and reduced to metallic form upon it. Since the deposition takes place atom-by-atom, it can be used to seal very small areas.

The main steps of the fabrication process are described in Fig. 5.2a. A 500 µm thick double side polished <100> cut silicon wafer was used as a substrate for atom trapping chip. A 3 µm thick oxide was grown on both sides of the wafer to form an electrically insulating layer. The feedthroughs were defined by UV lithography (150 µm x 150 µm square) and etched through silicon by using $80°C$, 30 % KOH solution (in DI water) . A titanium adhesion layer and a copper seed layer (30nm and 200 nm, respectively) were thermally evaporated on both sides of the substrate and inside the feedthroughs. The current carrying wires (100 µm wide) were patterned by UV lithography on both sides and 12 µm thick copper is electroplated to make the wires thick enough to stand high current necessary for condensation in such a configuration. A photoresist was then used to define the areas where the copper electroplating was utilized to seal the feethroughs. To totally seal feedthroughs, 10-12 hour electroplating was necessary. Consequently, the adhesion layer and the copper seed layer were stripped off by wet etching. The final step was to UV pattern and etch away (20 % hydrogen fluoride) the oxide layer. This was necessary for realizing the anodic bonding between the chip and a glass cell of the portable vacuum

system.

A sideview of the resulting feedthroughs is shown in Fig. 5.2b. As can be seen, the result for electroplating is not perfect, and some voids are visible within the feedthroughs. Consequently, some of the feedthoughs exhibited vacuum leaking after anodic bonding to a glass cell. The observed problem was attributed to the residual photoresist within the feedthroughs even after the UV exposure and its development.
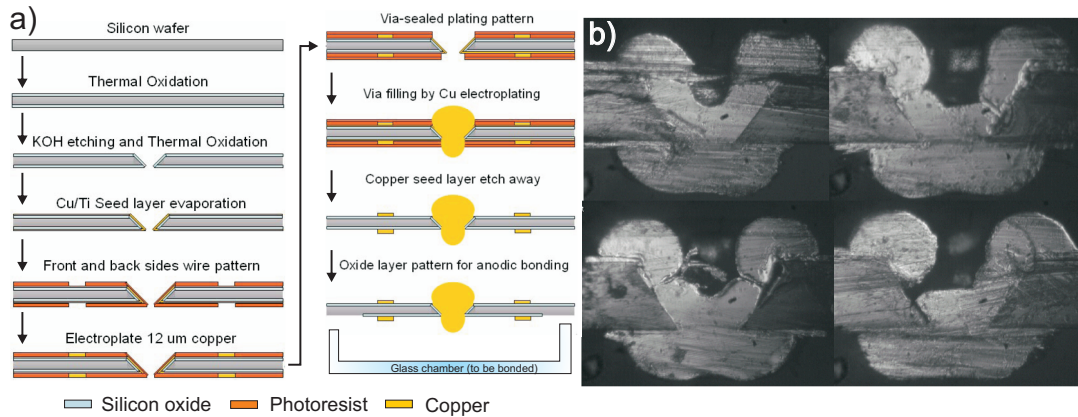

FIGURE 5.2 a) Fabrication steps for atom trapping chips (first approach). b) Sideview of the fabricated feedthroughs. Modified from the paper **V** of this thesis.

To verify the assumption, an alternative fabrication approach was introduced, where the feedthroughs were protected from UV resist by simply adding a piece of tape prior to photoresist spinning. The main steps of the process are described in Fig. 5.3a, and the sideview of the resulting feedthroughs in 5.3b. As can be seen, the resulting electroplated copper appears very uniform without any voids.
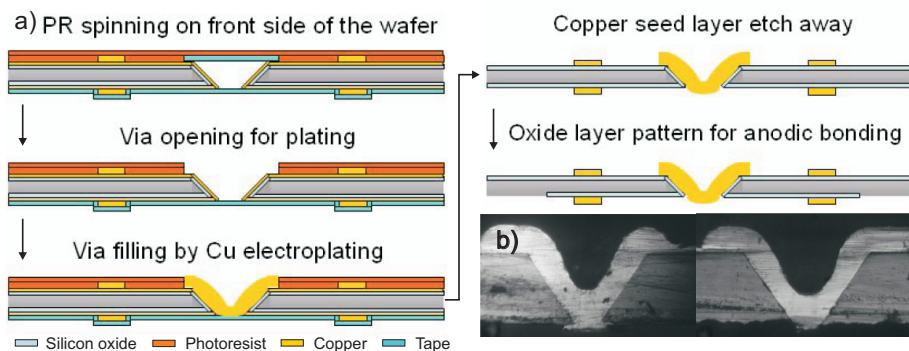

FIGURE 5.3 a) Fabrication steps for atom trapping chips (second approach). b) Sideview of the fabricated feedthroughs. Modified from the paper **V** of this thesis.

In Figs. 5.4a and b are shown the photographs of feedthrough atom trapping chip which then was anodically bonded to a Pyrex 7740 glass cell for Bose-Einstein

condensate experiments see Figs. 5.4c and d. After the anodic bonding step, the vacuum seal by a helium vacuum detector and the current carrying characteristics was further tested.
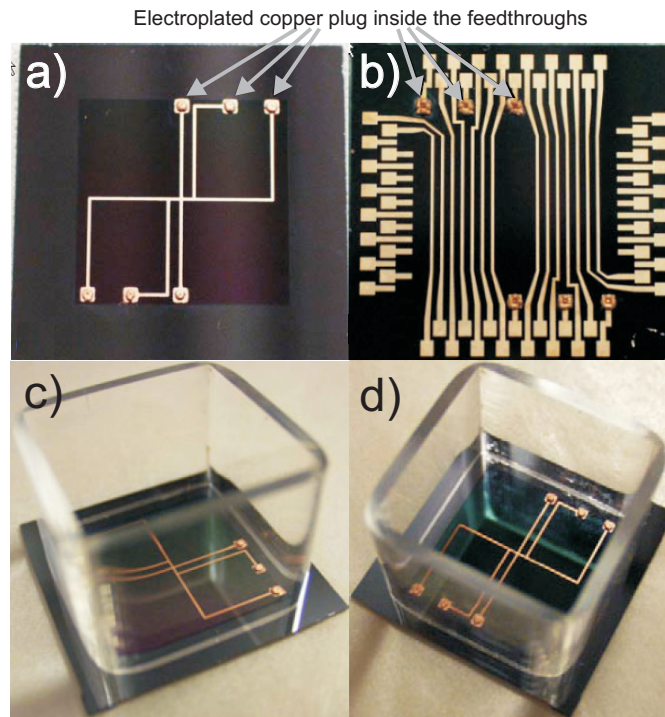

FIGURE 5.4 Photographs of feedthrough atom trapping chip anodically bonded to a Pyrex 7740 glass cell for Bose-Einstein condensate experiments. Modified from the paper **V** of this thesis.

Interestingly, while such a configuration enables to scale down the BEC to micronscale, a novel method for nanoscale BEC was recently suggested, which utilizes *surface plasmons* [57]. While currently a great effort is given to minimize SPP losses, in this case the losses are *utilized* to realize Bose-Einstein condensate of atoms. In this context, SPPs are used to introduce a viscous damping force through ohmic losses that facilitates the loading of the trap with atoms. Further, SPPs enable the miniatyrization of Bose-Einstein condensate to nanoscale by overcoming the attractive van der Waals force near material surfaces.

To summarize, a novel fabrication process for feedthrough atom trapping chips for atomic optics experiments was developed and successfully tested by a helium vacuum detector on the electroplated feedthoughs and anodically bonded areas. No leaking was detected during testing at 1×10^{-9} torr and room temperature. Later, by improvement in the substrate cleaning procedure, a yield of 97 % was achieved, even after the anodic bonding step, which requires the heating of the feedthroughs up to 425 °C [19].

Chapter 6

Summary

Weak coupling between molecules and SPP. The papers **I** and **II** and the section **II** of this thesis discuss molecular interaction with surface plasmon polaritons in the weak coupling regime. In this limit, the characteristic emission and absorption features of the molecules are not significantly changed as compared to vacuum conditions. A photon-SPP-photon conversion is demonstrated in the paper **I**, in which the incoupling and the outcoupling, which are spatially separated by 10 μm, is realized by using molecules. The paper **II** demonstrates that by utilizing the vibrational relaxation of R6G or SR101 molecules, a frequency conversion for propagating SPPs can be realized. Further, QDs were shown to couple the photons to SPPs.

Strong coupling between molecules and SPP. Strong coupling between SPPs and R6G molecules was demonstrated in paper **III** and section **III** of this thesis. In this regime, also qualitative features, such as spectral shape, are strongly modified with respect to vacuum conditions. In contrast to previous reports [9, 74] it was also shown that all three energy branches of the strongly coupled SPP-molecular excitation hybrid system can be converted into photons. Two novel detection methods were introduced, revealing features of the system time evolution that are not visible in conventional angle resolved reflection spectroscopy used in previous studies [9, 74]. Also, a quantum mechanical hybridization of the two molecular excitations and SPP was reported for the first time. Finally, in analogy to tunable-Q optical microcavities, it was shown that the Rabi splitting can be controlled by adjusting the interaction time between waveguided SPPs and R6G deposited on top of the waveguide. The interaction time can be controlled with sub-fs precision by adjusting the length of the R6G area with standard lithography methods, allowing studies of extremely nonadiabatic phenomena in strongly coupled systems.

Field induced nanolithography. In paper **IV** and section **IV** of this thesis, a novel method is demonstrated for high throughput, high precision pattern transfer for nanoscale objects by utilizing dynamically controllable electric field patterns on a master stamp. The proof-of-principle experiment here was done using quantum dots. High throughput, high-accuracy fabrication of arrayed quantum dots is of ma-

jor importance as such, for instance in the context of solar cells and optical biosensors. In general, the method can be readily extended for trapping of various other nano-objects in addition to quantum dots. Due to the demonstrated extreme robustness of the method, it is likely that the limits of performance can be pushed even much further. An important advantage of using dielectrophoresis in pattern transfer is based on the fact that, in addition to high precision and high throughput, the method enables dynamic control over the trapping and transferred pattern; one single universal master stamp can be used to generate any desired multicomponent pattern to the target plate. Due to its robustness, versatility and universality, the method has remarkable application potential in nanotechnology.

Ultra high vacuum compatible electrical feedthroughs for portable Bose-Einstein condensate setup. The paper **V** and section **V** presents a method for fabricating ultra high vacuum compatible electrical feedthroughs for atom trapping chip used to create Bose-Einstein condensates. The method takes advantage of the electroplating technology together with the mass fabrication capabilities inherent in UV lithography. The method enables to fabricate on-chip ultra high vacuum sealable feedthroughs, small enough to have dozens of them on a single chip, but large enough to stand high currents necessary for the realization of BEC in such a configuration.

Bibliography

[1] AGRANOVICH, V., BENISTY, H., AND WEISBUCH, C., *Organic and inorganic quantum wells in a microcavity: Frenkel-Wannier-Mott excitons hybridization and energy transformation*. Solid State Commun. **102** (1997) 631.

[2] AGRANOVICH, V. M., LITINSKAIA, M., AND LIDZEY, D. G., *Cavity polaritons in microcavities containing disordered organic semiconductors*. Phys. Rev. B **67** (2003) 085311.

[3] AKIMOV, A. V., MUKHERJEE, A., YU, C. L., CHANG, D. E., ZIBROV, A. S., HEMMER, P. R., PARK, H., AND LUKIN, M. D., *Generation of single optical plasmons in metallic nanowires coupled to quantum dots*. Nature **450** (2007) 402.

[4] ANDERSON, M. H., ENSHER, J. R., MATTHEWS, M. R., WIEMAN, C. E., AND CORNELL, E. A., *Observation of Bose-Einstein Condensation in a Dilute Atomic Vapor*. Science **269** (1995) 198.

[5] ANDREANI, L. C., PANZARINI, G., AND GÉRARD, J.-M., *Strong-coupling regime for quantum boxes in pillar microcavities: Theory*. Phys. Rev. B **60** (1999) 13276.

[6] BALYKIN, V. I., KLIMOV, V., AND LETOKHOV, V. S., *Atom Nanooptics Based on Photon Dots and Photon Holes*. JETP Lett **78** (2003) 8.

[7] BARNES, W. L., *Topical review Fluorescence near interfaces: the role of photonic mode density*. Journal of Modern Optics **45** (1998) 661.

[8] BARNES, W. L., DEREUX, A., AND EBBESEN, T. W., *Surface plasmon subwavelength optics*. Nature **424** (2003) 824.

[9] BELLESSA, J., BONNAND, C., PLENET, J. C., AND MUGNIER, J., *Strong Coupling between Surface Plasmons and Excitons in an Organic Semiconductor*. Phys. Rev. Lett. **93** (2004) 036404.

[10] BOJARSKI, P., *Concentration quenching and depolarization of rhodamine 6G in the presence of fluorescent dimers in polyvinyl alcohol films*. Chemical Physics Letters **278** (1997) 225.

[11] BOLLER, K.-J., IMAMOLU, A., AND HARRIS, S. E., *Observation of electromagnetically induced transparency*. Phys. Rev. Lett. **66** (1991) 2593.

[12] BOSE, S. N., *Plancks Gesetz und Lichtquantenhypothese*. Z. Phys. **26** (1924) 178.

[13] CHANG, D. E., SORENSEN, A. S., DEMLER, E. A., AND LUKIN, M. D., *A single-photon transistor using nanoscale surface plasmons*. Nature Physics **3** (2007) 807.

[14] CHANG, Y., HUANG, S., AND CHEN, Y., *Biomolecular Nanopatterning by Electrophoretic Printing Lithography*. Small **5** (2009) 63.

[15] CHIOU, P. Y., OHTA, A. T., AND WU, M. C., *Massively parallel manipulation of single cells and microparticles using optical images*. Nature **436** (2005) 370.

[16] CHIOU, P. Y. AND WU, M. C., *Manipulating Nanoparticles and Macromolecules with Light Patterned Microfluidic Flow*. Proceedings of the 3rd IEEE Int. Conf. on Nano/Micro Engineered and Molecular Systems (2008) 1204.

[17] CHOU, S. Y., KEIMEL, C., AND GU, J., *Ultrafast and direct imprint of nanostructures in silicon*. Nature **417** (2002) 835.

[18] CHOU, S. Y., KRAUSS, P. R., AND RENSTROM, P. J., *Imprint Lithography with 25-Nanometer Resolution*. Science **272** (1996) 85.

[19] CHUANG, H.-C., ANDERSON, D. Z., AND BRIGHT, V. M., *The fabrication of through-wafer interconnects in silicon substrates for ultra-high-vacuum atom-optics cells*. J. Micromech. Microeng. **18** (2008) 045003.

[20] COHEN, A. E., *Control of Nanoparticles with Arbitrary Two-Dimensional Force Fields*. Phys. Rev. Lett. **94** (2005) 118102.

[21] DANCKWERTS, M. AND NOVOTNY, L., *Optical Frequency Mixing at Coupled Gold Nanoparticles*. Phys. Rev. Lett. **98** (2007) 026104.

[22] DIENEROWITZ, M., MAZILU, M., , REECE, P. J., KRAUSS, T. F., AND DHOLAKIA, K., *Optical vortex trap for resonant confinement of metal nanoparticles*. Optics Express **16** (2008) 4991.

[23] DU, S. W., SQUIRES, M. B., IMAI, Y., CZAIA, L., SARAVANAN, R. A., BRIGHT, V. M., REICHEL, K., HANSCH, T. W., AND ANDERSON, D. Z., *Bose-Einstein Condensation in a Portable Vacuum Cell*. Phys. Rev. A **70** (2004) 053606.

[24] EINSTEIN, A., *Quantentheorie des einatomigen idealen Gases*. Sitzungsberichte der Preussischen Akademie der Wissenschaften **1924** (1924) 261.

[25] FAIST, J., CAPASSO, F., SIRTORI, C., WEST, K. W., AND PFEIFFER, L., *Controlling the sign of quantum interference by tunnelling from quantum wells*. Nature **390** (1997) 589.

[26] FASEL, S., ROBIN, F., MORENO, E., ERNI, D., GISIN, N., AND ZBINDEN, H., *Energy-Time Entanglement Preservation in Plasmon-Assisted Light Transmission*. Phys. Rev. Lett. **94** (2005) 110501.

[27] FERMANI, R., SCHEEL, S., AND KNIGHT, P. L., *Trapping cold atoms near carbon nanotubes: Thermal spin flips and Casimir-Polder potential*. Phys. Rev. A **75** (2007) 062905.

[28] FLEISCHHAUER, M., IMAMOGLU, A., AND MARANGOS, J. P., *Electromagnetically induced transparency: Optics in Coherent Media*. Reviews of Modern Physics **77** (2005) 633.

[29] GUNTER, G., ANAPPARA, A. A., HEES, J., SELL, A., BIASIOL, G., SORBA, L., LIBERATO, S. D., CIUTI, C., TREDICUCCI, A., LEITENSTORFER, A., AND HUBER, R., *Sub cycle switch on of ultrastrong light matter interaction*. Nature **458** (2009) 178.

[30] HANSEL, W., HOMMELHOFF, P., HANSCH, T. W., AND REICHEL, J., *Bose-Einstein Condensation on A Microelectronic Chip*. Nature **413** (2001) 498.

[31] HARRIS, S. E., FIELD, J. E., AND IMAMOGLU, A., *Nonlinear optical processes using electromagnetically induced transparency*. Phys. Rev. Lett. **64** (1990) 1107.

[32] HAU, L. V., HARRIS, S. E., DUTTON, Z., AND BEHROOZI, C. H., *Light speed reduction to 17 metres per second in an ultracold atomic gas*. Nature **397** (1999) 594.

[33] HAYWARD, R. C., SAVILLE, D. A., AND AKSAY, I. A., *Electrophoretic assembly of colloidal crystals with optically tunable micropatterns*. Nature **404** (2000) 56.

[34] HOBSON, P. A., BARNES, W. L., LIDZEY, D. G., GEHRING, G. A., WHITTAKER, D. M., SKOLNICK, M. S., AND WALKER, S., *Strong exciton-photon coupling in a low-Q all-metal mirror microcavity*. Appl. Phys. Lett. **81** (2002) 3519.

[35] HOLMES, R. AND FORREST, S., *Strong exciton-photon coupling in organic materials*. Organic Electronics **8** (2006) 77.

[36] HOLMES, R. J. AND FORREST, S. R., *Strong Exciton-Photon Coupling and Exciton Hybridization in a Thermally Evaporated Polycrystalline Film of an Organic Small Molecule*. Phys. Rev. Lett. **93** (2004) 186404.

[37] HOUDRÉ, R., WEISBUCH, C., STANLEY, R. P., OESTERLE, U., PELLANDINI, P., AND ILEGEMS, M., *Measurement of Cavity-Polariton Dispersion Curve from Angle-Resolved Photoluminescence Experiments*. Phys. Rev. Lett. **73** (1994) 2043.

[38] Hsu, K. H., Schultz, P. L., Ferreira, P. M., and Fang, N. X., *Electrochemical Nanoimprinting with Solid-State Superionic Stamps*. Nano Letters **7** (2007) 446.

[39] Hughes, M. P., *AC electrokinetics: applications for nanotechnology*. Nanotechnology **11** (2000) 124.

[40] Hwang, J., Pototschnig, M., Lettow, R., Zumofen, G., Renn, A., Götzinger, S., and Sandoghdar, V., *A single-molecule optical transistor*. Nature **460** (2000) 76.

[41] Ishizaki, K. and Noda, S., *Manipulation of photons at the surface of three-dimensional photonic crystals*. Nature **460** (2009) 367.

[42] J. P. Burke, J., Chu, S.-T., Bryant, G. W., Williams, C. J., and Julienne, P. S., *Designing neutral-atom nanotraps with integrated optical waveguides*. Phys. Rev. A **65** (2002) 043411.

[43] Jauffred, L., Richardson, A. C., and Oddershede, L. B., *Three-Dimensional Optical Control of Individual Quantum Dots*. Nano Letters **8** (2008) 3376.

[44] Jones, T. B., *Basic theory of dielectrophoresis and electrorotation*. IEEE EMBS Magazine **22** (2003) 33.

[45] Kraus, T., Malaquin, L., Schmid, H., Riess, W., Spencer, N. D., and Wolf, H., *Nanoparticle printing with single-particle resolution*. Nature Nanotechnology **2** (2007) 570.

[46] Kumar, S., Seo, Y.-K., and Kim, G.-H., *Manipulation and trapping of semiconducting ZnO nanoparticles into nanogap electrodes by dielectrophoresis technique*. Appl. Phys. Lett. **94** (2009) 53104.

[47] Lamprecht, B., Krenn, J. R., Schider, G., Ditlbacher, H., Salerno, M., Felidj, N., Leitner, A., Aussenegg, F. R., and Weeber, J. C., *Surface plasmon propagation in microscale metal stripes*. Appl. Phys. Lett. **79** (2001) 51.

[48] Lee, H. J., Yasukawa, T., Suzuki, M., Taki, Y., Tanaka, A., Kameyama, M., Shiku, H., and Matsue, T., *Rapid fabrication of nanoparticles array on polycarbonate membrane based on positive dielectrophoresis*. Sensors and Actuators B **131** (2008) 424.

[49] Lee, J., Hernandez, P., Lee, J., Govorov, A. O., and Kotov, N. A., *Exciton-plasmon interactions in molecular spring assemblies of nanowires and wavelength-based protein detection*. Nature Materials **6** (2007) 291.

[50] LIDZEY, D., WENUS, J., WHITTAKER, D., ITSKOS, G., STAVRINOU, P., BRADLEY, D., AND MURRAY, R., *Hybrid polaritons in strongly coupled microcavities: experiments and models*. Journal of Luminescence **110** (2004) 347.

[51] LIDZEY, D. G., BRADLEY, D. D. C., ARMITAGE, A., WALKER, S., AND SKOLNICK, M. S., *Photon-Mediated Hybridization of Frenkel Excitons in Organic Semiconductor Microcavities*. Science **288** (2000) 1620.

[52] LIDZEY, D. G., BRADLEY, D. D. C., SKOLNICK, M. S., VIRGILI, T., WALKER, S., AND WHITTAKER, D. M., *Strong exciton-photon coupling in an organic semiconductor microcavity*. Nature **395** (1998) 53.

[53] LIDZEY, D. G., BRADLEY, D. D. C., VIRGILI, T., ARMITAGE, A., SKOLNICK, M. S., AND WALKER, S., *Room Temperature Polariton Emission from Strongly Coupled Organic Semiconductor Microcavities*. Phys. Rev. Lett. **82** (1999) 3316.

[54] LIDZEY, D. G., FOX, A. M., RAHN, M. D., SKOLNICK, M. S., AGRANOVICH, V. M., AND WALKER, S., *Experimental study of light emission from strongly coupled organic semiconductor microcavities following nonresonant laser excitation*. PHYSICAL REVIEW B **65** (2002) 195312.

[55] MAIER, S. A., KIK, P. G., ATWATER, H. A., S. MELTZER, A. A. R., AND KOEL, B. E., *Observation of coupled plasmon-polariton modes of plasmon waveguides for electromagnetic energy transport below the diffraction limit*. Proceedings of SPIE **4810** (2002) 71.

[56] MICHLER, P., KIRAZ, A., BECHER, SCHOENFELD, W. V., PETROFF, P. M., ZHANG, L., HU, E., AND IMAMOLU, A., *A Quantum Dot Single-Photon Turnstile Device*. Science **290** (2009) 2282.

[57] MURPHY, B. AND HAU, L. V., *Electro-Optical Nanotraps for Neutral Atoms*. Phys. Rev. Lett. **102** (2009) 033003.

[58] NIE, S. AND EMORY, S. R., *Probing Single Molecules and Single Nanoparticles by Surface-Enhanced Raman Scattering*. Science **275** (1997) 1102.

[59] NIKOLAJSEN, T., LEOSSON, K., AND BOZHEVOLNYI, S. I., *Surface plasmon polariton based modulators and switches operating at telecom wavelengths*. Appl. Phys. Lett. **85** (2004) 5833.

[60] NOGINOV, M. A., ZHU, G., MAYY, RITZO, B. A., NOGINOVA, N., AND PODOLSKIY, V. A., *Stimulated Emission of Surface Plasmon Polaritons*. Phys. Rev. Lett. **101** (2008) 226806.

[61] OLYMPUS, *Basic Concepts in Fluorescence.* http://www.olympusmicro.com/ primer/techniques/fluorescence/fluorescenceintro.html (accessed October 2009).

[62] OTT, H., FORTAGH, J., SCHLOTTERBECK, G., GROSSMANN, A., AND ZIMMERMANN, C., *Bose-Einstein Condensation in a Surface Microtrap.* Phys. Rev. Lett. **87** (2001) 230401.

[63] POHL, H. A., *Dielectrophoresis: The Behavior of Neutral Matter in Nonuniform Electric Fields* (Cambridge University Press: Cambridge, U.K., 1978).

[64] PURCELL, E. M., BLOEMBERGEN, N., AND POUND, R. V., *Resonance Absorption by Nuclear Magnetic Moments in a Single Crystal of CaF$_2$.* Phys. Rev. **70** (1946) 988.

[65] REITHMAIER, J. P., SEK, G., LÖFFLER, A., HOFMANN, C., KUHN, S., REITZENSTEIN, S., KELDYSH, L. V., KULAKOVSKII, V. D., REINECKE, T. L., AND FORCHEL, A., *Strong coupling in a single quantum dot-semiconductor microcavity system.* Nature **432** (2004) 197.

[66] RIGHINI, M., ZELENINA, A. S., GIRARD, C., AND QUIDANT, R., *Parallel and selective trapping in a patterned plasmonic landscape.* Nature Physics **3** (2007) 477.

[67] RONDELEZ, Y., TRESSET, G., NAKASHIMA, T., FUJITA, Y. K.-Y. H., TAKEUCHI, S., AND NOJI, H., *Highly coupled ATP synthesis by F1-ATPase single molecules.* Nature **433** (2005) 773.

[68] ROTHEMUND, P. W. K., *Folding DNA to create nanoscale shapes and patterns.* Nature **440** (2006) 297.

[69] SHIM, J. S., YUN, Y.-H., RUST, M. J., DO, J., SHANOV, V., SCHULZ, M. J., AND AHN, C. H., *High precision fluidic alignment of carbon nanotubes using magnetic attraction on a metal catalyst.* MEMS 2008, Tucson, AZ, USA, January 13-17 (2008) 729.

[70] SKOLNICK, M. S., FISHER, T. A., AND WHITTAKER, D. M., *Strong coupling phenomena in quantum microcavity structures.* Semicond. Sci. Technol. **13** (1998) 645.

[71] SONG, J., ATAY, T., SHI, S., URABE, H., AND NURMIKKO, A. V., *Large enhancement of fluorescence efficiency from CdSe/ZnS quantum dots induced by resonant coupling to spatially controlled surface plasmons.* Nano letters **5** (2005) 1557.

[72] SUGAWARA, Y., KELF, T. A., BAUMBERG, J. J., ABDELSALAM, M. E., AND BARTLETT, P. N., *Strong Coupling between Localized Plasmons and Organic Excitons in Metal Nanovoids.* Phys. Rev. Lett. **97** (2006) 266808.

[73] SUZUKI, M., YASUKAWA, T., SHIKU, H., AND MATSUE, T., *Negative Dielectrophoretic Patterning with Colloidal Particles and Encapsulation into a Hydrogel*. Langmuir **23** (2007) 4088.

[74] SYMONDS, C., BELLESSA, J., PLENET, J. C., BRÉHIER, A., PARASHKOV, R., LAURET, J. S., AND DELEPORTE, E., *Emission of hybrid organic-inorganic exciton/plasmon mixed states*. Appl. Phys. Lett. **90** (2007) 091107.

[75] SYMONDS, C., BONNAND, C., PLENET, J. C., BRÉHIER, A., PARASHKOV, R., LAURET, J., DELEPORTE, E., AND BELLESSA, J., *Particularities of surface plasmon-exciton strong coupling with large Rabi splitting*. New Journal of Physics **10** (2008) 065017.

[76] VIJAYARAGHAVAN, A., BLATT, S., WEISSENBERGER, D., ORON-CARL, M., HENNRICH, F., GERTHSEN, D., HAHN, H., AND KRUPKE, R., *Ultra-Large-Scale Directed Assembly of Single-Walled Carbon Nanotube Devices*. Nano Lett. **7** (2007) 1556.

[77] WAINSTAIN, J., DELALANDE, C., GENDT, D., VOOS, M., BLOCH, J., THIERRY-MIEG, V., , AND PLANEL, R., *Dynamics of polaritons in a semiconductor multiple-quantum-well microcavity*. Phys. Rev. B **58** (1998) 7269.

[78] WEISBUCH, C., NISHIOKA, M., ISHIKAWA, A., AND ARAKAWA, Y., *Observation of the coupled exciton-photon mode splitting in a semiconductor quantum microcavity*. Phys. Rev. Lett. **69** (1992) 3314.

[79] WINELAND, D. J., DRULLINGER, R. E., AND WALLS, F. L., *Radiation-pressure cooling of bound resonant absorbers*. Phys. Rev. Lett. **40** (1978) 1639.

[80] YOSHIE, T., SCHERER, A., HENDRICKSON, J., KHITROVA, G., GIBBS, H. M., RUPPER, G., ELL, C., SHCHEKIN, O. B., AND DEPPE, D. G., *Vacuum Rabi splitting with a single quantum dot in a photonic crystal nanocavity*. Nature **432** (2004) 200.

[81] ZAYATS, A. V. AND I. I. SMOLYANINOV, A. A. M., *Nano-optics of surface plasmon polaritons*. Physics Reports **408** (2005) 131.

[82] ZHENG, L., BRODY, J. P., AND BURKE, P. J., *Electronic manipulation of DNA, proteins, and nanoparticles for potential circuit assembly*. Biosensors and Bioelectronics **20** (2004) 606.

[83] ZIA, R. AND BRONGERSMA, M. L., *Surface plasmon polariton analogue to Youngs double-slit experiment*. Nature Nanotechnology **2** (2007) 426.